PARALLEL AND UNSTRUCTURED COMPUTATION OF 2-D AND 3-D VORTEX FLOWS

by

Oğuz Dayı

B.S. in M.E., İstanbul Technical University, 2002

Submitted to the Institute for Graduate Studies in
Science and Engineering in partial fulfillment of
the requirements for the degree of
Master of Science

Graduate Program in Graduate Program in Mechanical Engineering

Boğaziçi University

2005

PARALLEL AND UNSTRUCTURED COMPUTATION OF 2-D AND 3-D VORTEX FLOWS

APPROVED BY:

Assist. Prof. Ali Ecder .....
(Thesis Supervisor)

Assoc. Prof. Can Özturan .....
(Thesis Co-supervisor)

Assist. Prof. Kunt Atalık .....

Assist. Prof. Hasan Bedir .....

Prof. Levent Kurnaz .....

DATE OF APPROVAL: 1/9/2005

to the labour of my parents and lecturers, Oğuz Dayı

ACKNOWLEDGEMENTS

Firstly I would like thank to my advisors Dr. Ali Ecder and Dr. Can Özturan who gave me opportunity to work on this thesis. Thank's so much to my family for their support during the whole thesis period. Additionally I wish to thank to Dr. Akın Tezel and Dr. Kunt Atalık who helped me so much. Finally i thank especially to Ali Haydar Özer, Mustafa Özer Gelişli, Ali Ök and Mehmet Orhan who encouraged and tried to helped me in various steps of this study with their wealthy and valuable knowledge.

ABSTRACT

PARALLEL AND UNSTRUCTURED COMPUTATION OF 2-D AND 3-D VORTEX FLOWS

Vortex flows are main flows which lead to turbulence phenomenon. Turbulence is a complicated and many-faceted problem of fluid dynamics. These flows have striking and varied spatial organizations. Nearly every flow that can be observed in nature has turbulent character. Consequently, engineering systems in various applications are affected by turbulence. Significant examples of such cases are severe efficiency decreases of pumps and turbines which are designed for a specific design load. There are many cases in combustion or mixing applications where the high mixing and heat-transfer rates of the turbulent boundary layer are desirable. So, better understanding of turbulent flow regimes requires further investigation of vortex flows. Consistent with this purpose, several groups of study were performed to cover different types of vortex flows within the context of this study.

Firstly, a basic vortex flow is analyzed with various numerical techniques in this study. This test problem is lid driven cavity flow. An implicit finite volume discretization technique is used in terms of primitive variables for the unstructured code. Unstructured grids are handled with staggered grid arrangement for irregular domains in 2D. Fractional step method is used as a velocity-pressure coupling.

Finally, in addition to these analysis Taylor vortex flows in two different 3D geometries and 3D Centrifugal Pump flow analysis are conducted with the aid of various turbulence models. LES (Large Eddy Simulation), k-epsilon, k-omega turbulence models are used. Analysis that are mentioned above is conducted with parallel processing technique.

ÖZET

İKİ VE ÜÇ BOYUTLU GİRDAPLI AKIŞLARIN PARALEL VE YAPISAL OLMAYAN ÇÖZÜM AĞI İLE HESABI

Girdaplı akışlar, türbülanslı akışlara yol açan başlıca akış türüdürler. Türbülanslı akışkanlar kompleks ve çok yüzlülüğe sahip akışkanlar mekaniği problemidir. Bu akışlar çarpıcı ve çeşitli uzaysal organizasyonlara sahiptirler. Doğada görülen hemen her akış türbülans karakterine sahiptir. Bunun sonucu olarak birçok mühendislik uygulaması türbülans tarafından etkilenmektedir. Bu durumların en çarpıcı olanları pompa ve türbinlerin belli bir yükleme noktası için tasarlanmış verimlerindeki düşüşlerdir. Türbülanslı sınır tabakalarındaki yüksek karışım ve ısı transferi değişim oranlarının özellikle istenildiği birçok yanma ve karışım uygulamaları mevcuttur. Bu nedenlerden dolayı türbülanslı akışların daha iyi anlaşılabilmesi, vorteks akışların daha detaylı incelenmesini gerektirmektedir. Belirtilen amaca uyumlu olmak üzere bu çalışma kapsamında, çok farklı vorteks akışları incelemek üzere dört farklı çalışma yapılmıştır.

İlk olarak, bu çalışmada değişik nümerik teknikler kullanılarak bir temel girdap akışı incelenmiştir. Bu akış kapak tahrikli akışıdır. Yapısal olmayan çözüm ağını esas alan yazılım için ilkel değişkenler üzerinden kapalı sonlu hacimler yöntemi ile ayrıştırma yapılmıştır. Yapısal olmayan çözüm ağ yapısı iki boyutta düzgün olmayan geometriler için şaşırtmalı ağ yapısı düzeninde gerçekleştirilmiştir. Kademeli bölme metodu hız-basınç karşılıklı bütünlemesi için kullanılmıştır.

Son olarak, yukardaki analizlere ek olarak; değişik türbülans modellerinin kullanıldığı, iki farklı üç boyutlu geometride Taylor girdap akışları ile santrifüj pompa akış analizleri gerçekleştirilmiştir. LES (Büyük Girdap Simülasyonu), k-ϵ, k-w türbülans modelleri kullanılmıştır. Analizlerin birçoğu parallel olarak gerçekleştirilmiştir.

TABLE OF CONTENTS

LIST OF FIGURES

LIST OF TABLES

LIST OF SYMBOLS

A_o	Constant for C_μ in k-ϵ realizable model
$A(t)$	Amplitude history of the maximum streamline in mid plane
A_1	Constant for C_μ in k-ϵ realizable model
C_μ	Dynamic turbulent viscosity constant
C_p	Cost of parallel processing
C_s	Smagorinsky constant
$C_{1\epsilon}$	Model Constant for k-ϵ modeling
$C_{2\epsilon}$	Model Constant for k-ϵ modeling
d	Annular width (mm)
D_w	Cross diffusion term for w
E	Wall function constant ≈9.793
E_p	Efficiency of parallel processing
f	Physical quantity
$\overline{f}$	Mean of physical quatitiy over a space or time
f'	Fluctuation of physical quatitiy
$\vec{F^c}$	Vectorial form of convective fluxes
$\vec{F^v}$	Vectorial form of diffusive fluxes
G_b	Generation of turbulence kinetic energy due to buoyancy ($\frac{m^2}{s^2}$)
G_k	Generation of turbulence kinetic energy due to the mean velocity gradients ($\frac{m^2}{s^2}$)
G_w	Generation of w
$G_\Delta(x,\zeta)$	Filtering functions
i	Index for the x-direction
j	Index for the y-direction
k	Turbulent kinetic energy ($\frac{m^2}{s^2}$)
L	Characteristic length (mm)
M	Preconditioning matrix
p_∞	Ambient pressure (pa)
Re	Reynolds number

Re_t	Turbulent Reynolds number
Re_1	Reynolds number of inner cylinder or torus
Re_2	Reynolds number of outer cylinder or torus
p	Dimensional pressure (pa)
$p^{'}$	Non-dimensional pressure
r_i	Inner radius (mm)
r_o	Outer radius (mm)
S_ϵ	Source term for ϵ
S_k	Source term for k
S_{ij}	Large strain rate tensor
S_w	Source term for w
t	Time (s)
Ta	Taylor Number
$t^{'}$	Non-dimensional time
$t_i^{'}$	Initial time for the ensemble averaging (s)
t_p	Execution time for parallel processing (s)
t_s	Execution time for sequential processing (s)
u	Velocity of x direction ($\frac{m}{s}$)
u_∞	Free stream velocity ($\frac{m}{s}$)
u_i^*	Tentative velocity in index form
$u^{'}$	Non-dimensional velocity of x direction
U^*	Non-dimensional group for velocity
v	Velocity of y direction($\frac{m}{s}$)
$v^{'}$	Non-dimensional velocity of y direction
V	Velocity in vectorial form($\frac{m}{s}$)
$< V(t) >$	Ensemble average ($\frac{m}{s}$)
$\overline{V}_i$	Time average ($\frac{m}{s}$)
w	Specific dissipation rate (frac1s)
w_k	Angular velocity ($\frac{rad}{s}$)
w	Velocity of z direction($\frac{m}{s}$)
$\vec{W}$	Vectorial form of a quantity for finite volume representation

y^*	Non-dimensional group for distance
y_ν	Physical viscous sublayer thickness (m)
y_ν^*	Constant for the non-equilibrium wall function y_ν ≈11.225
Y_M	Contribution of the fluctuating dilatation in compressible turbulence to the overall ϵ $(\frac{m^2}{s^3})$
Y_w	Dissipation of w
τ	Initial time for the time averaging (s)
Ω_1	Angular velocity of inner cylinder $(\frac{rad}{sn})$
Ω_2	Angular velocity of outer cylinder $(\frac{rad}{sn})$
Ω_a	Average angular velocity between inner and outer cylinder$(\frac{rad}{s})$
θ	Angle of spherical coordinates
η	Annular gap
ν	Kinematic viscosity $(\frac{m^2}{s})$
μ	Dynamic viscosity $(\frac{kg}{m.s})$
ρ	Density $(\frac{kg}{m^3})$
ρ_∞	Free stream density $(\frac{kg}{m^3})$
ϵ	Dissipation rate $(\frac{m^2}{s^3})$
μ_t	Dynamic turbulent viscosity $(\frac{kg}{ms})$
σ_k	Turbulent Prandtl number for k
σ_ϵ	Turbulent Prandtl number for ϵ
Ω	Vorticity $(\frac{1}{s})$
Ω_c	Space occupied with the control volume (m^2)
$\overline{\Omega}_{ij}$	Mean rotation tensor viewed in a rotating reference
τ_w	Wall shear stress $(\frac{kg}{ms^2})$
$\tilde{U}$	Mean velocity sensitized to pressure gradients $(\frac{m}{s})$
κ	von K$a^{'}$rm$a^{'}$n constant ≈0.4187
Γ_k	Effective diffusivity for k $(\frac{kg}{ms})$
Γ_w	Effective diffusivity for w $(\frac{kg}{ms})$
α_*	Low Reynolds correction coefficient for k-w SST model
τ_{ij}	subgrid scale tensor

Ψ	Stream function ($\frac{m^3}{s}$)
Δf	Filter width
Δ_i	Local mesh spacing in direction i where i=1,2,3
Ψ'	Dimensionless stream function
Ω'	Dimensionless vorticity
κ_m	m dimensional subspace
$\mathcal{L}_m$	m dimensional subspace where κ_m subspace projected
λ	Wavelength
$f()$	Terms of function
$O()$	Terms of order
$()_P$	Any quatitiy associated with spatial position P in space
$\nabla\,()$	Gradient operator
$\nabla .()$	Divergence operator
$\nabla^2\,()$	Laplacian operator

1. INTRODUCTION

Fluid flows are present everywhere in nature and are widely experienced by those people who observe nature with open eye. Evidently, it can be easily recognized that many processes in our natural environment are essentially dependent on the convective transport of heat and mass. Hence, without fluid motion, life on earth in the form we know it on could not exist.

Turbulence with an infinite scale exists in environmental studies which are meteorology, oceanography and astronomy. The boundary layer in earth's atmosphere is turbulent except where extreme stable conditions exist. Jet streams in the upper troposphere are turbulent; cumulus clouds are in turbulent motion. Anyone who observes flow of water in rivers and canals can easily finds that these flows are turbulent. The water currents below the surface of the ocean and rivers are also turbulent. Unique demonstration of this kind of turbulent flow is Gulf Stream. Gulf Stream is itself a turbulent wall-jet kind of flow. Turbulence can even be observed in outer space. The photosphere of the sun and photospheres of similar stars are in turbulent motion; interstellar gas clouds(gaseous nebulae) are turbulent. Currently there is a research that wake of the earth in solar wind is a turbulent wake [1].

The technical importance of fluid flows is also easily observable in many engineering fields where heat and mass transfer processes are strongly controlled by fluid motions. Most combustion processes involve turbulence. The flow of natural gas and oil in pipelines is turbulent. A study of turbulent flows is also important in combustion where enhancement in mixing of chemical species are needed. Chemical engineers use turbulence to mix and homogenize fluid mixtures to accelerate chemical reaction rates in liquid and gas enviroments. This technique is used in automobile engines to ensure an efficient combustion. Similarly, a good prediction of turbulent flow is also important for applications related to the aerodynamics of cars, trains and planes. Turbulent flow control finds numerous applications in aeronautics conjunction with drag reduction, thrust improvement, noise limitation, and increased freedom of movement.

Turbulent flows are in the context of more than one century in the time line of fluid mechanics. There are pioneers in this time line who made unique contributions to the investigation of turbulence but we have still have no unique model to simulate the turbulent flows today. Because of its complex nature, study of turbulent flows remains one of the most challenging problems of fluid mechanics. As a result, it continues to remain a research topic for the industry as well as the academic world [2].

Figure 1.1. Historical record of scientists contributing to the development of fluid mechanics [2].

All flows ranging from simple ones such as two dimensional jets, wakes, pipe flows and flat plate boundary layers to more complicated three dimensional ones become unstable above certain Reynolds number. These hydrodynamic instabilities lead to vortex formations. These vortices interact with the mean flow and extract energy from it. This is called vortex stretching. During these processes, rotation rate of the large vortices increase whereas radius of their cross-section decrease. This leads to energy transfer from large vortices to smaller vortices. These actions undergoes a chaotic transition regime and the fully developed turbulent character achieved [3].

Closer investigation of initial vortex formation and their interaction gains essential importance to predict the whole behavior of the turbulent flow. These vortex formations can occur with infinite number of ways depending on infinite number of factors. Geometry, boundary conditions and type of the fluid are the main factors that can be counted. Various kinds of vortex and turbulent flows are covered with different

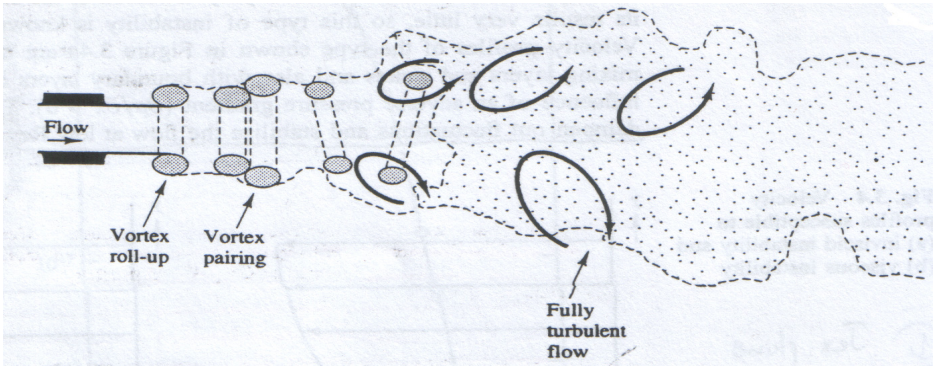

Figure 1.2. Turbulent flow formation [3].

numerical techniques in this study to investigate effect of these factors.

Decay of a simple eddy was studied as an introductory case. This subject was firstly studied by G. I. Taylor and H. A. Webb as indicated in reference [4]. The analytical solution of incompressible viscous fluid motion was an interesting and challenging scientific problem for these scientists. They thought that an analytical solution can be derived if the behavior of a simple eddy studied in a detailed way. Their study lead to important and fascinating results. The discussion of the properties of the eddy indicates that there is a slight analogy between the theory of eddies in a viscous fluid and the quantum theory of radiation. The analogy was constructed between the critical values of the angular momentum in Bohr's atomic theory with critical values of the Reynolds number in viscous fluid motion. The similarity is significant as the angular momentum has the same dimensions as Reynolds number multiplied by a mass. The mass quantity that is used to construct the analogy is electron mass and viscosity of the ether respectively. Another exact solution of the equations of motion of a viscous fluid yields a result which reminds one of the well known condition for instability in the case of a horizontally stratified atmosphere. The analytical solution they have introduced in equation 1.1, solution states very important results.

$$u = ke^{\lambda t - ky}cos(qx) \qquad ,v = ke^{\lambda t - ky}sin(qx) \tag{1.1}$$

Wavelength λ is defined by the following equality. Table 1.1 states the behavior of the solution in equation 1.1. Decaying eddy condition has been issued in this study.

$$\lambda = \nu(k^2 - q^2) \tag{1.2}$$

Table 1.1. Behavior of a vortex

$k = 0$	Irrotational flow
$k < q$	Decaying eddy
$k > q$	Motion is becoming more violent

The numerical setup of the problem is a set of Taylor vortex array which decay with time. One of the cell inside the Taylor vortex array focused on rather than to examine whole vortex array in this study. The decay of the vortex with time simulated. Results are compared by the analytical solution. One of the many fascinating instabili-

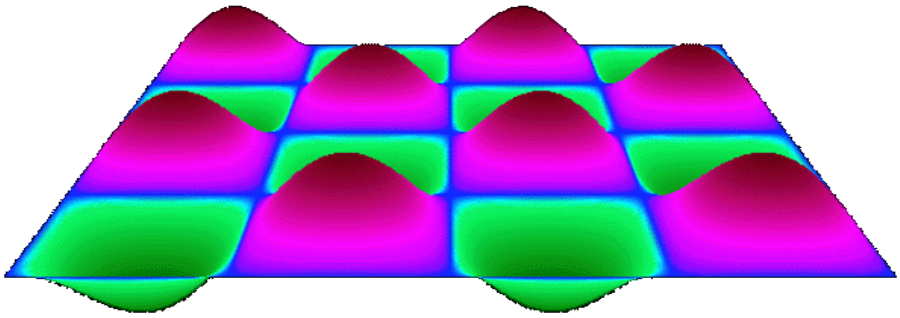

Figure 1.3. Taylor vortex array [6].

ties that occur in hydrodynamics is the formation of toroidal vortices in a fluid confined to an annular gap between concentric rotating cylinders. The phenomenon is named after Taylor, who carried out experimental studies and provided a hydrodynamic stability analysis of the effect [5]. Taylor quantitatively predicted and experimentally confirmed the existence of a flow instability when the inner cylinder reaches a critical speed. For low cylinder speeds, the fluid simply moves azimuthally around the cylinders. Taylor observed that when this simple flow becomes unstable, it is replaced by a cellular pattern in which the fluid travels in helical paths around the cylinders in layers of vortices known as Taylor Vortices. If the outer cylinder is taken to be

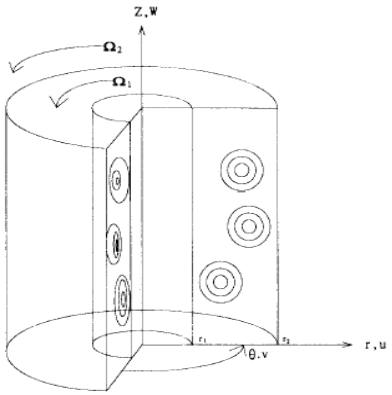

Figure 1.4. The geometry of the flow in cylindrical coordinates system. [7].

at rest, and the angular velocity of the inner cylinder is Ω_1, then the nature of the flow depends on the dimensionless Taylor number, Ta number defined according to the formula 1.3 Reynolds number defined according to kinematic viscosity, average angular velocity between inner cylinder and outer cylinder(Ω_a) and annular width denoted by d in equation 1.4.

$$Ta = \frac{{\Omega_a}^2 r_i d^3}{\nu^2} \tag{1.3}$$

$$Re = \frac{r_i w_a d}{\nu}, d = r_o - r_i, \tag{1.4}$$

Several researchers worked on this kind of flow instability after the pioneer research of G. I. Taylor, theoretically, experimentally and numerically. These researchers focused on different aspects of this flow. This is because the nonlinear behavior of each configuration leads to different vortex structures. These different flows had been identified taxonomically with respect to the increasing Taylor and Reynolds numbers and illustrated in maps.

Two important characteristics of the configuration shows its effect significantly. The flow with non-zero axial through flow leads to traveling Taylor vortices. The

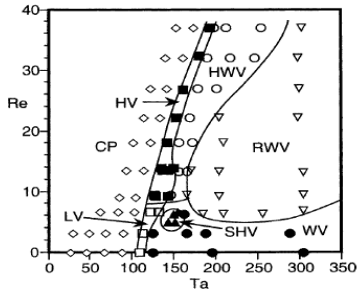

Figure 1.5. Flow regimes for cylindrical Couette flow with an imposed axial flow for η = 0.85. Symbols represent measurement points: CP=stable Couette Poiseuille flow; LV=laminar vortices; HV=helical vortices; HWV=helical wavy vortices; SHV=stationary helical vortices; WV=wavy vortices; RWV=random wavy vortices. (Reprinted with permission of AIP). [9].

second characteristic is the relation between the number of vortices and the size of the annular gap. We focused on the second parameter in this study.

Industrial applications of Taylor vortex flow takes place between the rotating surfaces of machinery, as well as in the operation of chemical engineering process equipment. The inclusion of a very small axial motion leads to plug-flow reactor. The yield of continuous reactors is maximized, if very good radial mixing is combined with minimal amount of longitudinal mixing. Such an ideal mixing environment can be obtained by annular flow through rotating concentric cylinders with Taylor vortex formation [8].

Taylor vortex flow tried to be extended to an analogical geometry for industrial application purposes. This application takes place in fluid couplings as seen by the figures 1.7, 1.8.

Torque that is created by an external electric motor is transformed by the primary side of the fluid coupling that is directly connected to the motor shaft directly into kinetic energy. This kinetic energy is converted again into mechanical energy by the secondary side of the coupling. No wear occurs and no mechanical contact of the power transmitting parts occurs The torque that is exerted to the secondary side increases with the cube of the input speed. The applications of these fluid couplings varies

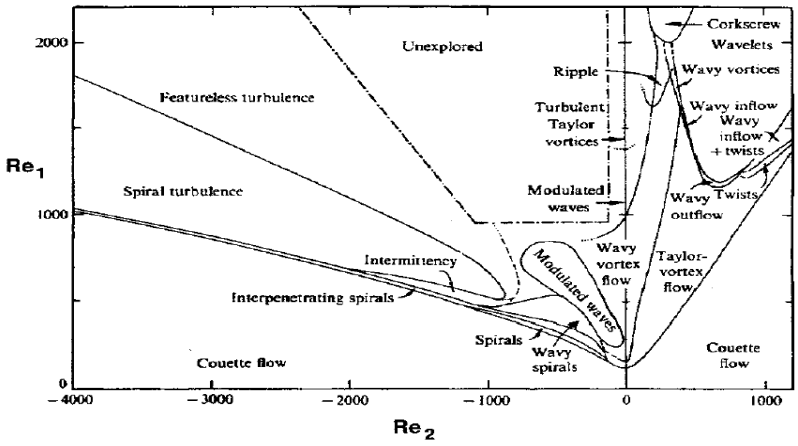

Figure 1.6. Phase diagram of flow states obtained by setting the outer cylinder speed and then slowly increasing the inner cylinder speed. The inner and outer cylinder speeds are expressed as Reynolds numbers Re_1 and Re_2, respectively, as defined in the text. The experimental system had radius ratio $\eta = 0.883$ and aspect ratio 30. [10].

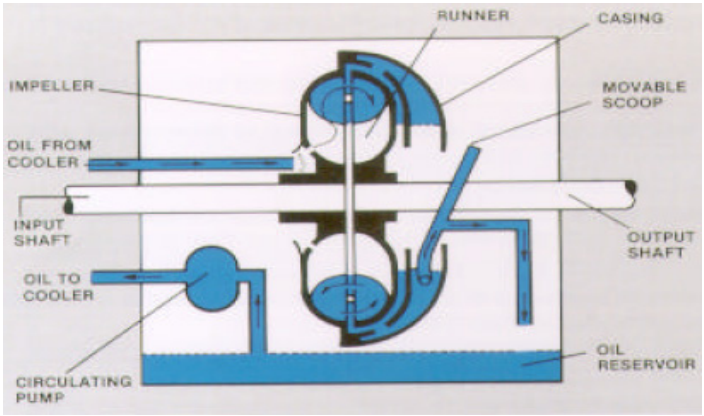

Figure 1.7. Fottinger fluid coupling [11]

extensively from hydraulic power transmission systems to retarder break systems and damping systems where huge amount of power applications take place.

Vortex formations on a simplified geometry has been analyzed. Simplified geometry constituted by a torus with annulus. Blade assembly had not been taken under considerations since the main goal in here is not to investigate the full system but to visualize the behavior of the general system to the given boundary conditions in terms of vortex flow. Torus divided into two equal parts. These parts are rotated with different speeds with respect to each other to obtain some vortex formations similar to Taylor Couette vortex flow between concentric cylinders.

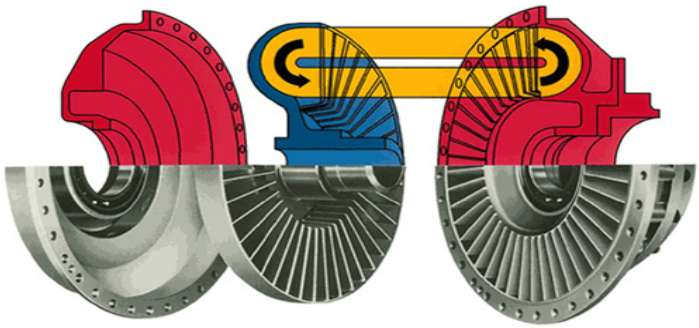

Figure 1.8. Transmission components [11].

Figure 1.9. An industrial application of fottinger fluid coupling [11].

Parallel processing technique has been conducted on the analysis of these vortex flows to demonstrate essential role of parallel processing. The demonstration made over different mesh sizes for different processor numbers. The time balance between message time and processing time discussed to mention where parallel processing is extremely important in the analysis of these kind of big numerical systems.

Another industrial application where vortex flows take place is in turbo machinery applications. The internal flow that develops in a centrifugal pump impeller is one of these flows and has this kind of character. Furthermore, flow is often influenced by rotor-stator interaction mechanisms or other unsteady effects. Vortex formations in the impeller passages cause dramatic decrease in the efficiency for design and off-design conditions. This is the major reason why fluid flows on these systems are still under investigation extensively both by experimentally and numerically.

These complex type of systems are analyzed by two very important experimental techniques which are Laser Doppler Velocimetry(LDV) and Particle Image Velocime-

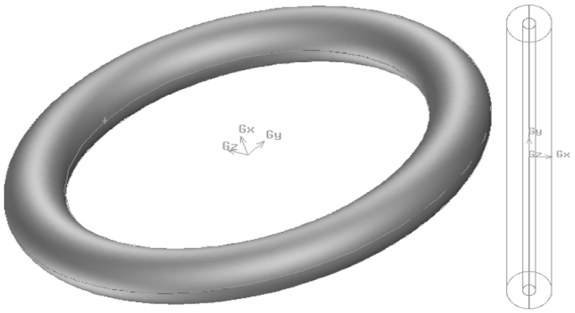

Figure 1.10. Simplified model for fotttinger fluid coupling

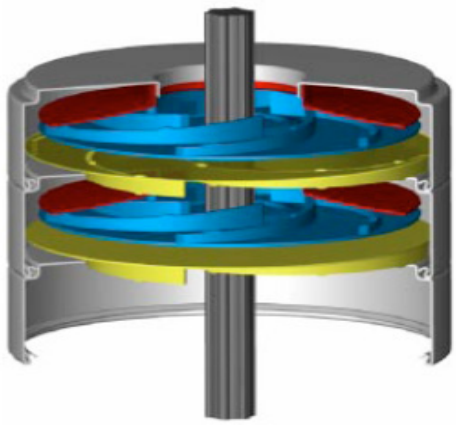

Figure 1.11. Two stages of an industrial multistage pump with the shrouded centrifugal pump [12].

try(PIV). These techniques found to be revealing extensive data about the complex behavior of these systems even in turbulent case.

There are several studies conducted over the centrifugal pumps for design and off design conditions by experimental studies. Akin and Rockwell [13] used PIV to work on the wake formation originate on a model impeller in a simulated rotating machine. They analyzed the interaction between stationary diffuser blade and this wake. Their work emphasized flow separation and reattachment events by instantaneous streamline patterns and vorticity contours. Eisele et al.[14] implemented another useful method called particle tracking velocimetry (PTV) to a vaned diffuser. They have found some interesting flow behavior. Flow separation in the diffuser channel and a recirculating backflow from the diffuser into the impeller at partial load conditions are some examples to these behaviors. Recently Sinha and Katz [15] and Sinha et al. [16] used PIV

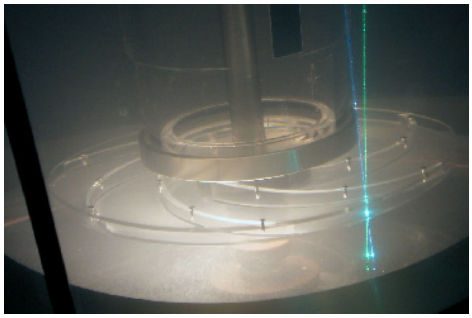

Figure 1.12. LDV measurement over a shrouded centrifugal pump [12].

technique for rotor-stator interactions between a centrifugal pump impeller and a vaned diffuser. They concluded with some flow structure and turbulence modeling issues. Oldenburg and Pap [17] performed PIV measurements in the impeller and in the volute of a purpose-made two-dimensional centrifugal pump. Data that is taken from the mid height cross section for three different orientations of the impeller. Some separations from the vanes are observed. This indicated a departure from potential flow patterns. Hayami et al. [18] and Aramaki and Hayami [19] applied PIV with a CCD(charge coupled device) camera which is rotating with the impeller with 30 rpm. They measured relative velocity and time dependent spatial variation of the impeller flow.

Some researchers also worked numerically on the impeller flows. These kind of works are however far less than experimental ones. The methodology in numerics which is considered to be sufficient enough to solve these kind of flows is the unsteady approach which resolves the vorticial and turbulent character development through time. There is technique called Large Eddy Simulation(LES) which uses this approach rather than steady approach for industrial applications. This technique is between RANS(Reynolds Averaged Navier Stokes) and DNS(Direct Numerical Simulation). LES takes advantage of high accuracy of DNS where appropriate and decreases the computational time by RANS properties. Computational time of these kind of systems are one of the major important factors in these kind of analysis [20].

Eggels [21] investigated the impact of a mechanical impeller on the turbulent flow field in a baffled stirred tank reactor using the Smagorinsky model and found good agreement with experimental data. Revstedt et al. [22] used implicit model to

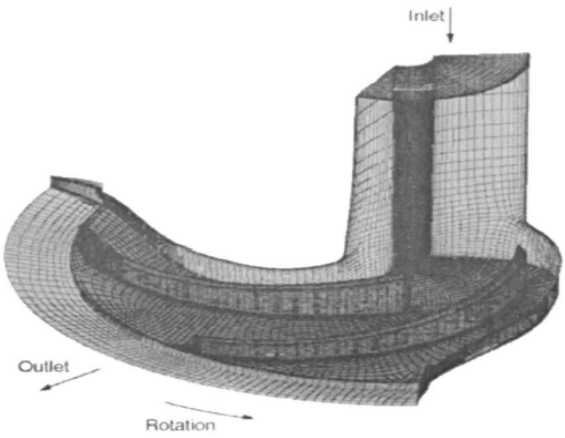

Figure 1.13. An example grid generated over a impeller stage [20].

solve similar systems and achieved coherent results of Eggels work. LES of the flow through the spiral casing, impeller, and exit section of a Francis turbine system at different operating conditions have been conducted by Chen and Song [24] giving first an insight into the flow field present in each unit separately and later also taking into account the mutual interaction between the rotating and stationary parts. Kato et al. [25] presented the first achievements of LES of the flow in a complete stage of a mixed flow pump at design flow percentage of 60 and 100. Again the Smagorinsky model was used. For both operating conditions the unsteady fluid forces on the impeller agreed well with measured values.

In this study a geometry ,which is nearly identical to the references [12],[20] is used as a model. Only design load case is analyzed. The time history of the system resolved with LES technique till steady state solution achieved. Good agreement achieved with respect to the references [12],[20] in terms of velocity field. The transient behavior of the system discussed. Coherent structures are extracted with a vortex identification method given in [44].

The core of this study focuses on the vortex flows with incorporation of variety of numerical methods. Code development has been performed within the context of this goal. Some important characteristics of the code is worthy to be stated. Code has the capability of using the unstructured grids for a future implementation of complex geometry applications. Code takes advantage of various Newton-Krylov techniques and

preconditioners that is used widely as advanced numerical techniques today. There are some new approaches that has been implemented in the code in terms of numerics with respect to the references from literature that will be cited in section 3.3 . Most important of these approaches is the implementation of a fractional step approach to a hybrid staggered numerical scheme with Newton-Krylov methods. Since this code development is not continuation of a previously written code, validation of the results was essential. One of the widely used benchmark tests has been implemented. This problem concerns the lid driven cavity for various *Re* numbers. Limits of the code has been detected where accuracy of the solver starts to have problems. Further numerical enhancements has been discussed. Parallel implementation of this test case with PETSc on ASMA cluster has been conducted also for the demonstration of parallelism. The schematics of this problem can be seen in the next figure.

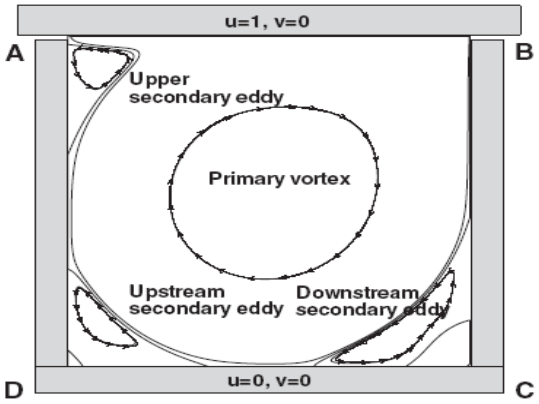

Figure 1.14. Lid cavity boundary conditions with the basic features of cavity flow [26].

2. MATHEMATICAL AND PHYSICAL MODELLING

Analysis of vortex flows starts with the identification of the relevant set of equations. Navier Stokes equations are the governing equations for this implementation, full set of these equations are given with the following in a conservative form [27].

Conservation of mass:

$$\frac{\partial(\rho)}{\partial t} + \nabla.(\rho V) = 0 \tag{2.1}$$

Conservation of x momentum:

$$\frac{\partial(\rho u)}{\partial t} + \frac{\partial(\rho u^2)}{\partial x} + \frac{\partial(\rho uv)}{\partial y} + \frac{\partial(\rho uw)}{\partial z} = -\frac{\partial p}{\partial x} + \frac{\partial}{\partial x}(\lambda \nabla.V + 2\mu \frac{\partial u}{\partial x}) \tag{2.2}$$

$$+ \frac{\partial}{\partial y}\left[\mu\left(\frac{\partial v}{\partial x} + \frac{\partial u}{\partial y}\right)\right] + \frac{\partial}{\partial z}\left[\mu\left(\frac{\partial u}{\partial z} + \frac{\partial w}{\partial x}\right)\right] + \rho f_x \tag{2.3}$$

Conservation of y momentum:

$$\frac{\partial(\rho v)}{\partial t} + \frac{\partial(\rho uv)}{\partial x} + \frac{\partial(\rho v^2)}{\partial y} + \frac{\partial(\rho vw)}{\partial z} = -\frac{\partial p}{\partial y} + \frac{\partial}{\partial x}\left[\mu\left(\frac{\partial v}{\partial x} + \frac{\partial u}{\partial y}\right)\right] \tag{2.4}$$

$$+ \frac{\partial}{\partial y}(\lambda \nabla.V + 2\mu \frac{\partial v}{\partial y}) + \frac{\partial}{\partial z}\left[\mu\left(\frac{\partial w}{\partial y} + \frac{\partial v}{\partial z}\right)\right] + \rho f_y \tag{2.5}$$

Conservation of z momentum:

$$\frac{\partial(\rho w)}{\partial t} + \frac{\partial(\rho uw)}{\partial x} + \frac{\partial(\rho vw)}{\partial y} + \frac{\partial(\rho w^2)}{\partial z} = -\frac{\partial p}{\partial z} + \frac{\partial}{\partial x}\left[\mu\left(\frac{\partial u}{\partial z} + \frac{\partial w}{\partial x}\right)\right] \tag{2.6}$$

$$+ \frac{\partial}{\partial y}\left[\mu\left(\frac{\partial w}{\partial y} + \frac{\partial v}{\partial z}\right)\right] + \frac{\partial}{\partial z}(\lambda \nabla.V + 2\mu \frac{\partial w}{\partial z}) + \rho f_z \tag{2.7}$$

There are 2D and 3D test problems covered within this study. The assumptions that are valid for each of these cases are given in the following chart:

- Flows considered to be incompressible for both 2D and 3D cases.
- Gravitational effects neglected for both 2D and 3D cases.
- Flows considered to be unsteady.
- No external force are induced inside the flow.

Governing equations simplify to the following vectorial form under the assumptions stated above.

Conservation of mass:

$$\vec{\nabla}.\vec{V} = 0 \tag{2.8}$$

Conservation of momentum:

$$\rho(\frac{\partial \vec{V}}{\partial t}) + \rho(\vec{V}.\vec{\nabla})\vec{V} = -\vec{\nabla}p + \mu\nabla^2\vec{V} \tag{2.9}$$

Although Navier Stokes equations seems to simplified in a very short form, when the Re number increases they become highly nonlinear with the convective terms. Beginning from the vortex formation to transient flow and finally to turbulent motion, flow field becomes extremely hard to predict. Some strategy can be introduced to identify these motions in terms of statistical point of view. Two ways of averaging the physical flow quantities is ensemble and time average which can be seen in the following equations consecutively:

Ensemble average:

$$< V(t) >= \lim_{N\to\infty} \frac{1}{N}\Sigma_{i=1,N} V(t_i' + t) \tag{2.10}$$

Time average for a finite T:

$$\overline{V}_i = \frac{1}{T}\int_{\tau}^{\tau+T} U_i(t+\tau).dt \tag{2.11}$$

Ensemble averages takes too much time but gives the realistic results. If $\overline{V}_i$ is independent of τ then process can be called stationary and time average can be used to average the quantities. If the time and ensemble averages coincide, the system is called ergodic. Vortex flows show good agreement with this concept, whereas it is not necessarily true for turbulent flows.

There are two approaches to solve these set of equations for the case of vortex and turbulent flows [28]. Both approaches have been conducted in this study for different

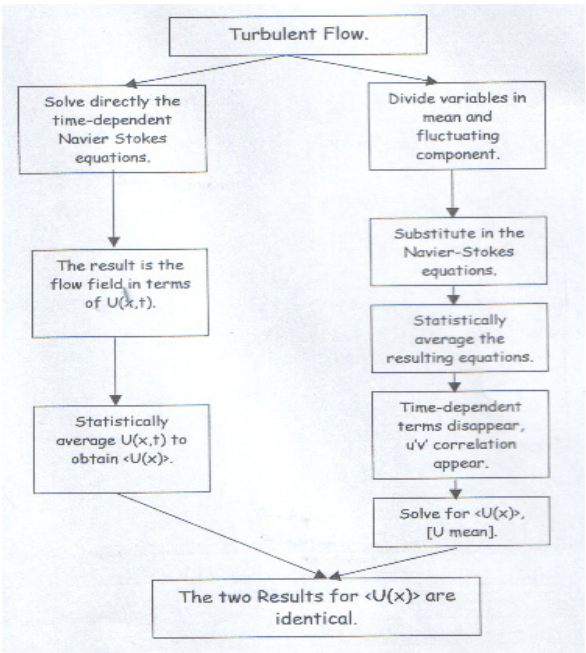

Figure 2.1. Approaches of solving vortex and turbulent flows [28].

case problems. Ensemble averaging is valid for the code development where small time steps regarding the physical time scale implemented to resolve the vortex formations. Code development on unstructured grids uses this approach. Reynolds decomposition which decompose the mean and fluctuating quantities has been implemented for the

3D cases. Taylor vortex flows have been analyzed with this approach. LES calculations on the centrifugal pump model is a bridge between these two techniques, which will be explained in section 2.5. Next section is devoted to the mathematical and physical modeling of RANS(Reynolds averaged Navier-Stokes) technique in terms of k-ϵ realizable with non-equilibrium wall functions and k-w SST modeling. k-ϵ modeling used for the concentric cylinder whereas k-w SST used for the concentric torus analysis respectively.

2.1. k-ϵ Standard Model

It is essential to introduce the basics of the standard k-ϵ model, which is derived semi-empirically, before going on the more complex models. This is because other models are obtained by upgrading the physics of this model by different approaches. Further discussion of theoretical basis can be found from the reference [29]. Two transport models are used for the k(turbulent kinetic energy) and ϵ(dissipation rate) respectively in k-ϵ modeling. Main assumptions of this model is to consider the flow as fully turbulent and neglect the molecular viscosity. Due to the fully turbulent assumption transitional effects are not available with this model. Two transport equations are given with following equations.

$$\frac{\partial(\rho k)}{\partial t} + \frac{\partial(\rho U_i k)}{\partial x_i} = \frac{\partial}{\partial x_j}\left[\left(\mu + \frac{\mu_t}{\sigma_k}\right)\frac{\partial k}{\partial x_j}\right] + G_k + G_b - \rho\epsilon - Y_M + S_k \tag{2.12}$$

$$\frac{\partial(\rho \epsilon)}{\partial t} + \frac{\partial(\rho U_i \epsilon)}{\partial x_i} = \frac{\partial}{\partial x_j}\left[\left(\mu + \frac{\mu_t}{\sigma_\epsilon}\right)\frac{\partial \epsilon}{\partial x_j}\right] + C_{1\epsilon}\frac{\epsilon}{k}\left(G_k + G_b\right) - C_{2\epsilon}\,\rho\frac{\epsilon^2}{k} + S_\epsilon \tag{2.13}$$

Turbulent viscosity calculated by the information of k and ϵ values that are maintained by the equations (2.12) (2.13). It is modeled according to expression (2.14)

where the C_μ is considered to be model constant.

$$\mu_t = \rho C_\mu \frac{k^2}{\epsilon} \tag{2.14}$$

There are different terms inside these equations which can be interpreted for some physical quantity. G_k represents the generation of turbulence kinetic energy due to the mean velocity gradients. G_b is the generation of turbulence kinetic energy due to buoyancy. Y_M represents the contribution of the fluctuating dilatation in compressible turbulence to the overall dissipation rate. $C_{1\epsilon}$ and $C_{2\epsilon}$ are model constants. σ_k and σ_ϵ are the turbulent Prandtl numbers for k and ϵ, respectively. S_k and S_ϵ are source terms.

The Navier Stokes equations are not closed due to the new unknowns induced by the Reynolds stress terms and model constants. The constants in the model has to be determined by the experimental data and given by the following:

Table 2.1. Standard k-ϵ model

$C_{1\epsilon}$	1.44
$C_{2\epsilon}$	1.92
$C_{2\mu}$	0.09
σ_k	1.0
σ_ϵ	1.0

2.2. k-ϵ Realizable Model

k-ϵ realizable model derived over standard model by forcing the model to satisfy certain mathematical constraints on the normal stresses, consistent with the physics of turbulent flows. In the case of eddy viscosity definition (2.14) and Boussinesq relationship (2.15) manipulated mathematically to obtain a relation for the Reynolds stress

terms with equation 2.16.

$$\overline{\rho u_i' u_j'} = \mu_t(\frac{\partial u_i}{\partial x_j} + \frac{\partial u_j}{\partial x_i}) - \frac{2}{3}(\rho k + \mu_t \frac{\partial u_i}{\partial x_i})\delta_{ij} \tag{2.15}$$

$$\overline{\rho u^2} = \frac{2}{3}k - 2\nu_t \frac{\partial U}{\partial x} \tag{2.16}$$

This last equation says that if the shear stress is sufficiently high enough the Reynolds stresses,which conceptually cannot be negative with its definition, can be negative. This problem can be solved if C_μ is not a constant as it was in standard model but a variable quantity. The main difference of this model with respect to others is this property. The new C_μ definition is given with the following expression (2.17).

$$C_\mu = \frac{1}{A_o + A_s \frac{(kU^*)}{\epsilon}} \tag{2.17}$$

where,

$$U^* = \sqrt{S_{ij}S_{ij} + \widetilde{\Omega_{ij}}\widetilde{\Omega_{ij}}} \tag{2.18}$$

$$\widetilde{\Omega_{ij}} = \overline{\Omega_{ij}} - \epsilon_{ijk} w_k \tag{2.19}$$

The last quantity ($\overline{\Omega}_{ij}$) is the mean rate-of-rotation tensor viewed in a rotating reference frame with the angular velocity ω_k for rotating flows.

Another enhancement of this model is a new model equation for dissipation ϵ

based on the dynamic equation of the mean-square vorticity fluctuation. New equation has been derived for this model to handle spreading rate for axisymmetric jets. Equation for the turbulent kinetic energy is same with the k-ϵ standard model. New transport equation for ϵ is given as following. Model constants are also given by (table 2.2).

$$\frac{\partial(\rho\epsilon)}{\partial t}+\frac{\partial(\rho U_i\epsilon)}{\partial x_i}=\frac{\partial}{\partial x_j}\left[\left(\mu+\frac{\mu_t}{\sigma_\epsilon}\right)\frac{\partial\epsilon}{\partial x_j}\right]+\rho C_{1\epsilon}S_\epsilon-\rho C_{2\epsilon}\frac{\epsilon^2}{k+\sqrt{\nu\epsilon}}+C_{1\epsilon}\frac{\epsilon}{k}C_{3\epsilon}G_b+S_\epsilon \tag{2.20}$$

Table 2.2. Model Constants for k-ϵ realizable model

$C_{1\epsilon}$	1.44
$C_{2\epsilon}$	1.9
σ_k	1.0
σ_ϵ	1.2

2.3. Standard and Non Equilibrium Wall Functions for k-ϵ Models

There were different wall treatments available in the FLUENT software. Non-Equilibrium wall functions implemented for a higher accuracy near wall for k-ϵ realizable model which is used for the analysis of the Taylor vortex flows in concentric cylinders. Theoretical background of these wall function are given in sections 2.3.1 and 2.3.2. Comparison, with respect to the standard wall function will be emhasized.

2.3.1. Standard Wall Functions for k-ϵ Models

Standard wall functions defined according to value of y^* and U^* called non-dimensional groups. Definitions of these groups at a certain point P are given in the

equations 2.21, 2.22.

$$U^* \equiv \frac{U_P C_\mu^{\frac{1}{4}} k_P^{\frac{1}{2}}}{\frac{\tau_w}{\rho}} \tag{2.21}$$

$$y^* \equiv \frac{\rho U_P C_\mu^{\frac{1}{4}} k_P^{\frac{1}{2}} y_P}{\mu} \tag{2.22}$$

Table 2.3. Definitions of non-dimensional groups

κ	von $Ka'rma'n$ constant≈0.42
E	Emprical constant for≈9.793
U_P	Mean velocity of the fluid at point P
k_P	Turbulent kinetic energy of the fluid at point P
y_P	Distance from point P to the wall

If $y^* < 11.225$ the laminar stress-strain relationship(2.23) is used which models the near wall region that is given by the equation 2.23.

$$U^* = y^* \tag{2.23}$$

2.3.2. Non Equilibrium Wall Functions for k-ϵ Models

This wall function has two features with respect to standard wall functions. Firstly, log law is upgraded to be sensitive to the pressure gradient effects. The new expression can be seen in the 2.24.

$$\frac{\widetilde{U} C_\mu^{\frac{1}{4}} k^{\frac{1}{2}}}{\frac{\tau_w}{\rho}} = \frac{1}{\kappa} ln(E \frac{\rho C_\mu^{\frac{1}{4}} k^{\frac{1}{2}} y}{\mu}) \tag{2.24}$$

Pressure gradient effects on 2.24 can be directly seen in the term $\widetilde{U}$ by 2.25 which enables the wall function pressure sensitive. Final expression is a function of quantitiy called physical viscous sublayer thickness(y_υ), given by equation 2.26.

$$\widetilde{U} = U - \frac{1}{2}\frac{dp}{dx}[\frac{y_\nu}{\rho\kappa\sqrt{k}}ln(\frac{y}{y_\nu}) + \frac{y - y_\nu}{\rho\kappa\sqrt{k}} + \frac{y_\nu^2}{\nu}] \tag{2.25}$$

$$y_\nu \equiv \frac{\mu y_\nu^*}{\rho C_\mu^{\frac{1}{4}} k_P^{\frac{1}{2}}} \tag{2.26}$$

The second and important enhancement is the two layer approach to calculate the G_k which is needed to solve equation 2.12 and identify the value of average dissipation rate($\overline{\epsilon}$) near the the boundary cells.

2.4. k-w STT(Shear Stress Transport) Model

This model is reported to be better than both k-ϵ and other standard k-w models due to its capability to modify the definition of the turbulent viscosity with respect to the transport of the principal turbulent shear stress. Model associates the specific dissipation rate(w) rather than the dissipation rate. Specific dissipation rate defined as the rate of dissipation of turbulence kinetic energy in unit volume and time. The transport equations of the model is given by the following (2.27)(2.28) ;

$$\frac{\partial(\rho k)}{\partial t} + \frac{\partial(\rho u_i k)}{\partial x_i} = \frac{\partial(\Gamma_k \frac{\partial k}{\partial x_j})}{\partial x_j} + G_k - Y_k + S_k \tag{2.27}$$

$$\frac{\partial(\rho w)}{\partial t} + \frac{\partial(\rho u_i w)}{\partial x_i} = \frac{\partial(\Gamma_w \frac{\partial k}{\partial x_j})}{\partial x_j} + G_w - Y_w + D_w + S_w \tag{2.28}$$

Again different terms can be seen, each represent a physical quantity. These terms are G_k represents the generation of turbulence kinetic energy due to mean velocity gradients. G_w represents the generation of w. Γ_k and Γ_w represent the effective diffusivity of k and w, respectively. Y_k and Y_w represent the dissipation of k and w due to turbulence. D_w represents the cross-diffusion term. S_k and S_w are source terms.

Although there are several differences between this model and others in theoretical basis, there are two that are significantly important. Firstly the effective viscosity defined in a manner that definition of turbulent viscosity is flexible rather than its usual form. This expression is given with in (2.29).

$$\Gamma_k = \mu + \frac{\mu_t}{\sigma_k} \tag{2.29}$$

$$\Gamma_w = \mu + \frac{\mu_t}{\sigma_w} \tag{2.30}$$

$$\mu_t = \frac{\rho k}{w} \frac{1}{max[\frac{1}{\alpha_*}, \frac{\Omega F_2}{a_1 w}]} \tag{2.31}$$

Coefficient, denoted by α_* is called low Reynolds correction coefficient which depends on the turbulent Reynolds number. It damps the turbulent viscosity. Definition of this coefficient is given by (2.32).

$$\alpha_* = \alpha_\infty^* (\frac{\alpha_0^* + \frac{Re_t}{R_k}}{1 + \frac{Re_t}{R_k}}) \tag{2.32}$$

$$Re_t = \frac{\rho k}{\mu w} \tag{2.33}$$

These definitions shows mathematically that the turbulent viscosity value and definition will change inversely proportional with maximum value of the denominator of (2.31). This is established by low Reynolds correction coefficient and some blending functions (F_2) are used. As an example, if the α_* is low, which means flow is low Reynolds flow, the turbulent viscosity will decrease according to (2.31). As the value of α_* goes to 1, it is considered to have high reynolds number flow.

Second important modification is the D_w represents the cross-diffusion term. This term enables the $k-w$ SST model switch from $k-w$ modeling to $k-\epsilon$ modeling. This term mathematically given with (2.34).

$$D_w = 2(1 - F_1)\rho\sigma_{w,2} \tag{2.34}$$

Model constants are also given in the table 2.4.

Table 2.4. Model Constants for k-w SST model

$\sigma_{k,1}$	1.176	$\sigma_{w,1}$	2.0
$\sigma_{k,2}$	1.0	$\sigma_{w,2}$	1.168
a_1	0.31	$\beta_{i,1}$	0.075
$\beta_{i,2}$	0.0828	R_k	6

2.5. LES(Large Eddy Simulation) Modeling

Approaches that are emphasized above were depending on the Reynolds averaged Navier Stokes equations. There is another approach that is called LES(Large eddy simulation) which depends on the modeling of scales of vortex structures. There may occur small and large scale vortex structures that can occur in an such an example flow 2.2.

Basic approach is the separation of these scales in terms of grid size. Smaller scales which are beyond the grid resolution should be modeled with a universal model.

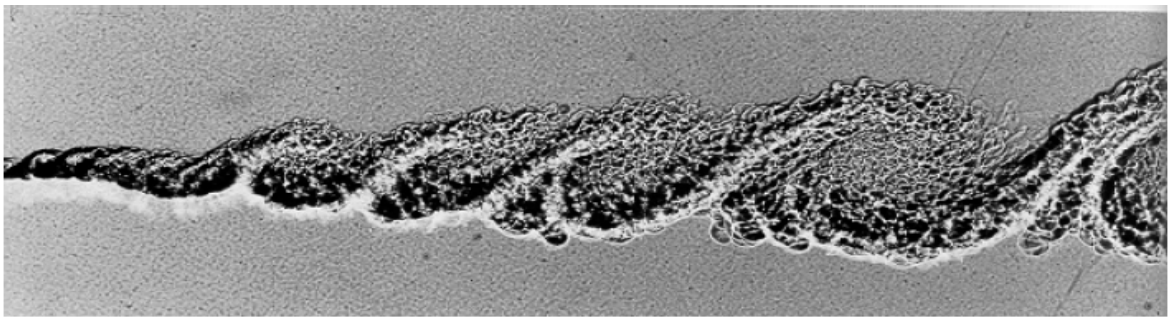

Figure 2.2. Scales of turbulence [30].

Larger scales that are bigger than the grid resolution should be computed on the grid. Filtering functions used to distinguish the large and smaller scales. Mean part of the quantities according to the reynolds decomposition are filtered according to the equation 2.35 with filtering equation $G_\Delta(x,\zeta)$ over domain D.

$$\overline{u}_i = \int_D G_\Delta(x,\zeta) u_i(\zeta) d\zeta \tag{2.35}$$

Introducing the filtering functions, filtered Navier-Stokes equations can be obtained. Filtered incompressible continuity and momentum equations are given in equations 2.36, 2.37.

$$\frac{\partial \overline{u}_i}{\partial x_i} = 0 \tag{2.36}$$

$$\frac{\partial \overline{u}_i}{\partial t} + \frac{\partial \overline{u}_i \overline{u}_j}{\partial x_j} = -\frac{\partial \overline{p}}{\partial x_i} + \frac{1}{Re}\frac{\partial^2 \overline{u}_i}{\partial x_i \partial x_j} - \frac{\partial \tau_{ij}}{\partial x_j} + \overline{f}_i \tag{2.37}$$

Unresolved smaller scales are called subgrid scales(SGS). The energy of these scales can be shown in a diagram 2.3 by the wave number in spectral space. These scales need to be modeled to close the filtered Navier-Stokes equations.

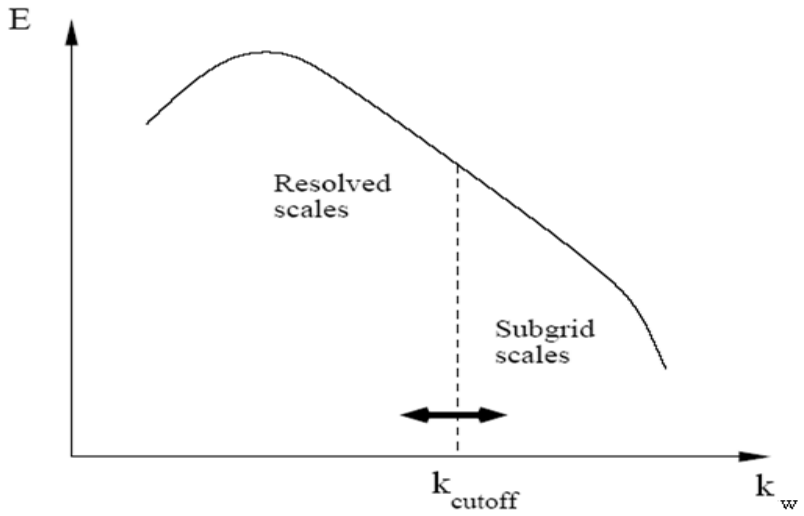

Figure 2.3. SGS(subgrid scales) in spectral space with respect to wave number [30].

SGS (Subgrid Scale) stresses defined by the expression 2.38.

$$\tau_{ij} = \overline{u_i u_j} - \overline{u}_i \overline{u}_j \tag{2.38}$$

Functionality associated by τ_{ij}, is to predict the small scale eddies from the resolved large eddy motion. This term can be decomposed into three different parts with the following [31].

$$\begin{aligned} \tau_{ij} &= L_{ij} + C_{ij} + R_{ij} && (2.39)\\ L_{ij} &= \overline{\overline{u}_i \overline{u}_i} - \overline{u}_i \overline{u}_j && (2.40)\\ C_{ij} &= \overline{\overline{u}_i u_j'} + \overline{u_j' \overline{u}_i} && (2.41)\\ R_{ij} &= \overline{u_i' u_j'} && (2.42) \end{aligned}$$

Following table shows the names of these terms.

Decomposed elements of SGS stresses	
L_{ij}	Leonard stresses
C_{ij}	Cross stresses
R_{ij}	Reynolds stresses of SGS

SGS modeling is especially important near the solid walls. The energy is absorbed from the large eddies to small eddies in these kind of regions so there is loss production of kinetic energy exist at this point. SGS model has to resolve this satisfactorily. If the transport equation written for the where q is the resolved kinetic energy.

$$\overline{q}^2 = \overline{u}_i \overline{u}_i \tag{2.43}$$

Transport equation for the q given by the equation 2.44.

$$\frac{\partial \overline{q}^2}{\partial t} + \frac{\partial \overline{q}^2 \overline{u}_j}{\partial x_i} = \frac{\partial}{\partial x_j}\left(-2\overline{pu}_j - 2\tau_{ij}\overline{u}_i + \frac{1}{Re}\frac{\partial \overline{q}^2}{\partial x_j}\right) - \frac{2}{Re}\frac{\partial \overline{u}_i}{\partial x_j}\frac{\partial \overline{u}_i}{\partial x_j} + 2\tau_{ij}\overline{S}_{ij} \tag{2.44}$$

The basic point in the modeling is the correlation of the subgrid stresses to large strain rate tensor . The correlation between these two established by the following expression:

$$\tau_{ij} = 2\nu_{SGS}\overline{S}_{ij} \tag{2.45}$$

$$\nu_{SGS} = C_s {\Delta_f}^2 \left|\overline{S}_{ij}\right| \tag{2.46}$$

$$\overline{S}_{ij} = \frac{1}{2}\left(\frac{\partial \overline{u}_i}{\partial \overline{x}_j} + \frac{\partial \overline{u}_j}{\partial \overline{x}_i}\right) \tag{2.47}$$

$$\Delta_f = (\Delta_1 \Delta_2 \Delta_3)^{\frac{1}{3}} \tag{2.48}$$

Main problem is the identification of C_s. This constant depends on the geometry and type of the flow that is under interest. It can be determined adaptively as reported in [32]. It is taken to be 0.09 in this study according to the reference paper that the geometry and setup of the problem taken [20].

3. COMPUTATIONAL MODELLING

Governing equations concerned in this study becomes highly nonlinear as the Re number increases. Vortex structures that originate by time inside the domain, add difficulty to solve the system that is under interest. Interaction of these structures even adds more nonlinearity by time.

Discretization of the governing equations are the first essential point that has to be considered. Finite difference and finite volume discretization methods are associated by the vortex problems via test problems in two separated code. Difference and behavior of these techniques are tried to be identified.

Finite difference discretication technique coupled by ADI(Alternating Direction Implicit) technique in terms of stream function-]. Tri-Diagonal Matrix Algorithm (TDMA) used as the solver.

Finite Volume discretization coupled with the fractional step techniques with preconditioning in terms of primitive variables. Powerful Newton-Krylov techniques accompanied by the preconditioning in a staggered grid approach used as the solver.

Another essential difference between these codes is the type of the grid that has been used. Structured grids used for the finite difference formulation whereas, unstructured grids used for the finite volume technique. Discussion of the finite difference and finite volume techniques will be stated in sections 3.1, 3.2 and 3.3.

3.1. Finite Difference Discretization and Stream Function - Vorticity Formulation

It is important to state the definitions of stream function(ψ) and vorticity(Ω) since finite difference calculations are conducted in terms of them.

$$u = \frac{\partial \psi}{\partial y} \tag{3.1}$$

$$v = -\frac{\partial \psi}{\partial x} \tag{3.2}$$

$$\Omega = \frac{\partial v}{\partial x} - \frac{\partial u}{\partial y} \tag{3.3}$$

It is possible to nondimensionalize these two definitions by the following expressions.

$$\psi^{'} = \frac{\psi L}{u_{\infty}} \tag{3.4}$$

$$\Omega^{'} = \frac{\Omega L}{u_{\infty}} \tag{3.5}$$

Stream function and vorticity definitions can be introduced into the governing equations of this study (equations 2.8 and 2.9) to obtain the stream function-vorticity formulation with nonconservative form in cartesian coordinates.

$$\frac{\partial \Omega^{'}}{\partial t} + u^{'}\frac{\partial \Omega^{'}}{\partial x^{'}} + v^{'}\frac{\partial \Omega^{'}}{\partial y^{'}} = \frac{1}{Re}\left(\frac{\partial^2 \Omega^{'}}{\partial {x^{'}}^2} + \frac{\partial^2 \Omega^{'}}{\partial {x^{'}}^2}\right) \tag{3.6}$$

$$\frac{\partial^2 \psi^{'}}{\partial {x^{'}}^2} + \frac{\partial^2 \psi^{'}}{\partial {x^{'}}^2} = -\Omega^{'} \tag{3.7}$$

Primitive variables in equations 3.6, 3.17 are nondimensionalized according to the following expressions. These expressions will be valid for the nondimensional form of the primitive variables in finite volume method implementation.

$$u^{'} = \frac{u}{u_{\infty}} \tag{3.8}$$

$$v^{'} = \frac{v}{u_{\infty}} \tag{3.9}$$

$$x^{'} = \frac{x}{L} \tag{3.10}$$

$$y^{'} = \frac{y}{L} \tag{3.11}$$

$$t^{'} = \frac{tu_{\infty}}{L} \tag{3.12}$$

$$Re^{'} = \frac{\rho_{\infty} u_{\infty} L}{\mu_{\infty}} \tag{3.13}$$

Navier-Stokes equations are decoupled into one elliptic equation and one parabolic equation which can be sequentially solved. This leads a one way coupling of these equations. Pressure term eliminated in these equations. Velocity field determined by this approach. It is not easy to implement the boundary conditions in terms of ψ and Ω. Furthermore, there is no simple stream function for the 3D cases [33]. This unfortunately indicates the flexibility limitation of this formulation.

Test case that was tested by this solver was Taylor vortex array and decay of adjacent process of adjacent vortices. Decay process of single eddy has been simulated by this technique. Since this is a decay process, only viscous terms can be taken under

interest. This leads the assumption of decomposition on the derivative of vorticity in equations 3.14 and 3.15. Convective terms vanish in equation 3.6 when this assumption inserted inside it. Decay process concerns the dissipation of the kinetic energy with the viscosity.

$$\frac{\partial \Omega'}{\partial x'} = \frac{\partial \Omega'}{\partial \psi'} \frac{\partial \psi'}{\partial x'} \tag{3.14}$$

$$\frac{\partial \Omega'}{\partial y'} = \frac{\partial \Omega'}{\partial \psi'} \frac{\partial \psi'}{\partial y'} \tag{3.15}$$

Governing equations that is under interest are given in the following simplified set of equations by these assumptions.

$$\frac{\partial \Omega'}{\partial t} = \frac{1}{Re} \left(\frac{\partial^2 \Omega'}{\partial {x'}^2} + \frac{\partial^2 \Omega'}{\partial {y'}^2} \right) \tag{3.16}$$

$$\frac{\partial^2 \psi'}{\partial {x'}^2} + \frac{\partial^2 \psi'}{\partial {y'}^2} = -\Omega' \tag{3.17}$$

Finite difference technique decompose the continuous domain into discrete points. Stream function-vorticity equations are discretized according to this decomposition. Discretization takes place on a certain stencil. Five point stencil is implemented for this study. Discretization has been conducted by ordinary central difference formulas which are derived by the taylor series expansion. Given a function $f(x)$ in a Δx change represented by the Taylor series expansion.

$$f(x + \Delta x) = f(x) + \Delta x \frac{\partial f}{\partial x} + \frac{(\Delta x)^2}{2!} \frac{\partial^2 f}{\partial x^2} + + \frac{(\Delta x)^3}{3!} \frac{\partial^3 f}{\partial x^3} + ... = f(x) + \sum_{n=1}^{\infty} \frac{(\Delta x)^n}{n!} \frac{\partial^n f}{\partial x^n} \tag{3.18}$$

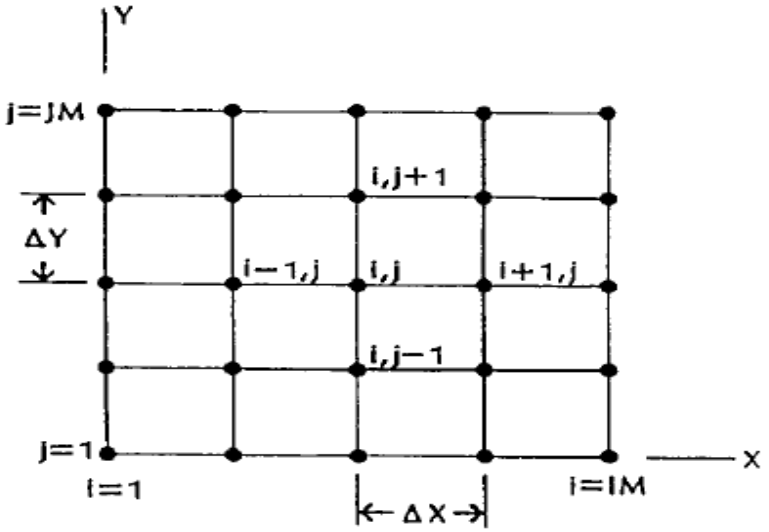

Figure 3.1. Five point stencil for structure grid [33].

Central differencing for the second order derivate s of diffusive terms defined by the previous and following nodes of the interested node. Mathematically this expressed with the following formula for second order accuracy($O(\Delta x^2)$ in x direction.

$$\frac{\partial^2 f}{\partial x^2} = \frac{f(x+\Delta x) - 2f(x) + f(x-\Delta x)}{(\Delta x)^2} + O(\Delta x)^2 \tag{3.19}$$

Temporal discretization made according to two consecutive nodes which are represented as previous(n) and next time($n+1$) to be solved.

$$\frac{\partial f}{\partial t} = \frac{f(x)^{n+1} - f(x)^n}{\Delta t} + O(\Delta t) \tag{3.20}$$

Discretized form of the equations 3.16 and 3.17 can be given by the aid of spatial and temporal discretizations in terms of indices dictated with figure 3.1.

$$\frac{\Omega_{i,j}^{n+1}-\Omega_{i,j}^{n}}{\Delta t}=\frac{1}{Re}\left(\frac{\Omega_{i+1,j}^{n+1}-2\Omega_{i,j}^{n+1}+\Omega_{i-1,j}^{n+1}}{(\Delta x)^2}+\frac{\Omega_{i,j+1}^{n+1}-2\Omega_{i,j}^{n+1}+\Omega_{i,j-1}^{n+1}}{(\Delta y)^2}\right)+O(\Delta t,\Delta x^2,\Delta y^2) \tag{3.21}$$

$$\frac{\psi_{i+1,j}^{n+1}-2\psi_{i}^{n+1}+\psi_{i-1,j}^{n+1}}{(\Delta x)^2}+\frac{\psi_{i,j+1}^{n+1}-2\psi_{j}^{n+1}+\psi_{i,j-1}^{n+1}}{(\Delta y)^2}=\Omega_{i,j}^{n+1} \tag{3.22}$$

This discretization coupled by the ordinary ADI numerical scheme. The resulting discretized equations solved by the TDMA solver. Implicit treatment of the numerical scheme has been conducted. Although, these techniques are well known techniques of CFD, they are relatively old and inefficient in terms of efficiency and robustness.

3.2. Finite Volume Discretization and Primitive Variables Formulation

Structured grids are good in terms of accuracy whereas their application needs transformation of the equations for geometries other than the rectangular domain. This constitutes the consideration of two grid systems. These are physical and computational grid systems which can be seen by the following double airfoil configuration example.

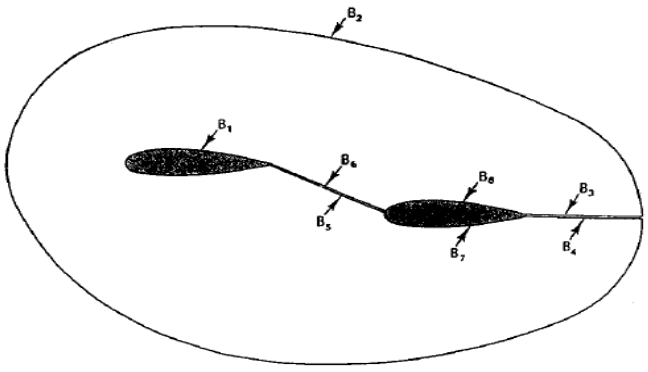

Figure 3.2. Physical domain of for a double airfoil [33].

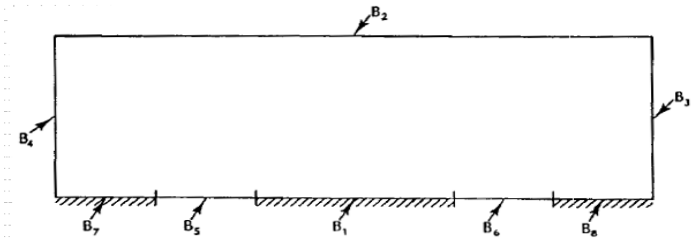

Figure 3.3. Computational domain of for a double airfoil [33].

There should be a connection between these two domains during the computations of the flow. This is only possible if the transformation of the governing equations in terms of metrics. This transformation established by the specifying a generalized coordinate system which will map the non rectangular grid system in the physical space to the rectangular computational space. This transformation is usually complex and hard to establish. In the case of stretching in certain regions, the implementation of this transformation becomes even much more harder for the complex physical domains. You should be also providing a physical grid system before establishing the transformation. Typical example of physical grid system for the double airfoil configuration is given in the next figure.

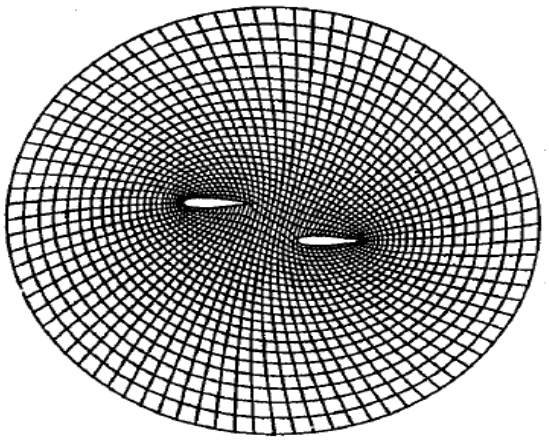

Figure 3.4. Physical grid on the double airfoil [33].

Unstructured grids are the alternative gateway to the complex geometry applications. Unstructured grid methods have become increasingly popular in the development of CFD technology to solve complex flow problems of industrial relevance. Within the unstructured grid method, the definition of a coordinate system is not necessary. Instead, a different data structure has to be adopted to handle geometrical data in figure

3.5.

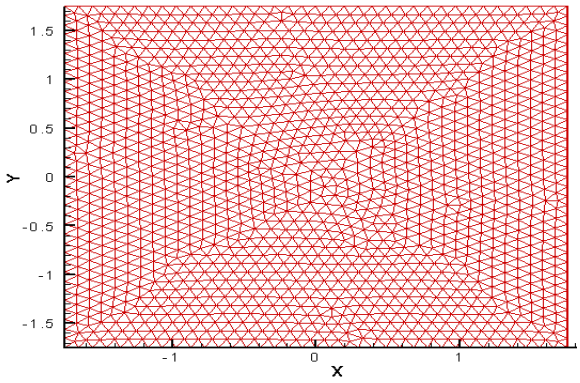

Figure 3.5. Unstructured grid

Design of this data structure is the essential point in the implementation of unstructure methods. It should be carrying the connectivity of grid points for any configurations both for interior and boundary cells while providing necessary but, not excessive information for the discretization. This makes the implementation of this technique very complex when compared with structure grids. Once this technique defined for the interior and boundary cells for any combination of the situation, it is possible to proceed with the complex geometries for future multi physics implementations.

In this study unstructured grids are implemented accompanied with the Finite Volume approach. Finite volume methods directly utilize the conservation laws with the integral formulation of the Navier-Stokes/Euler equations. It was first employed by McDonald[34] for the simulation of 2-D inviscid flows. Finite volume method discretized the governing equations by first dividing the physical space into a number of arbitrary polyhedral control volumes. This polynomial control volumes can take various shapes like given in the figure 3.6.

Finite volume technique states that conservation law for a general vector quantity(W) can be written in integral form for a continuous medium in equation 3.23 where

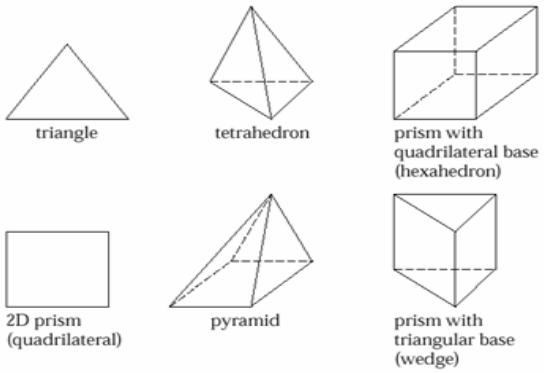

Figure 3.6. Different control volumes for unstructured grid application

$\vec{F_c}$ and $\vec{F_v}$ represent the convective and diffusive fluxes respectively [35].

$$\frac{\partial \vec{W}}{\partial t} = -\frac{1}{\Omega_c}\left[\oint_{\partial\Omega_c}(F_c - F_v)\,dS - \int_{\Omega_c}\vec{Q}d\Omega_c\right] \tag{3.23}$$

Time derivative of the conservative variables can be cast according to the following form in equation 3.24.

$$\frac{\partial}{\partial t}\int_{\Omega_c}\vec{W}d\Omega_c = \Omega_c\frac{\partial \vec{W}}{\partial t} \tag{3.24}$$

Integral form stated above, can be rewritten for the discrete domain in terms of finite volumes with the equation 3.25. The integration constitutes traveling over the the surfaces of the control volume with the aid of surface normals which can be seen in figure 3.7.

$$\frac{d\vec{W}}{dt} = -\frac{1}{\Omega_c}\left[\sum_{n=1}^{N_F}\left(\vec{F_c} - \vec{F_v}\right)\Delta S - \vec{Q}\Omega_c\right] \tag{3.25}$$

In this study triangle type has been used for 2D code development. It is essential to emphasize the governing equations and velocity-pressure coupling method to

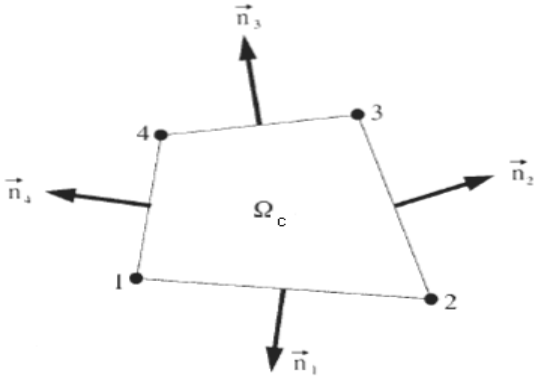

Figure 3.7. Control volume and surface normals

identify the associated data structure. Code development works in terms of primitive variables. Navier-Stokes equations in cartesian grid system are directly representing the governed equations independent of the geometry due to the unstructured grid system. Governed equations can be nondimensionalized according to 3.8-3.13. Additionally pressure nondimensionalized with the expression.

$$p^{'} = \frac{p}{\rho_{\infty} u_{\infty}} \tag{3.26}$$

Final form of the equations after manipulations can be given in index notation with equations 3.27 and 3.28.

Conservation of mass:

$$\frac{\partial u_i^{'}}{\partial x_i^{'}} = 0 \tag{3.27}$$

Conservation of momentum:

$$\frac{\partial u_i^{'}}{\partial t^{'}} + \frac{\partial (u_i^{'} u_j^{'})}{\partial x_j^{'}} = -\frac{\partial p^{'}}{\partial x_i^{'}} + \frac{1}{Re^{'}} \frac{\partial^2 u_i^{'}}{\partial x_j^{'} \partial x_j^{'}} \tag{3.28}$$

Velocity-pressure coupling is another aspect in finite volume formulation. Frac-

tional step method has been used which is suitable for incompressible methods. This method divides the computation of Navier-Stokes equations into predictor and corrector steps. Tentative velocity which is denoted as u_i^* in equation 3.29, is used in predictor step [36]. Calculated divergent free velocity field used to guess the pressure field with a poisson equation given by equation 3.30. Finally physical velocity corrected by combination of tentative and calculated non dimensional pressure field in equation 3.31.

$$\frac{u_i^* - u_i^{'n}}{\Delta t'} + \frac{\partial(u_j^{'n} u_j^*)}{\partial x_j'} = \frac{1}{Re'} \frac{\partial^2 u_i^*}{\partial x_j' \partial x_j'} \tag{3.29}$$

$$\frac{\partial^2 p^{'(n+1)}}{\partial x_j' \partial x_j'} = \frac{1}{\Delta t'} \frac{\partial u^*}{\partial x_i'} \tag{3.30}$$

$$u_i^{'(n+1)} = u_i^* - \Delta t' \frac{\partial p^{'(n+1)}}{\partial x'_i} \tag{3.31}$$

Discretization of the equations 3.29 and 3.30 should be regarded as another very important aspect of CFD which is called staggered grid approach. The discretization applied is again central differencing for finite volume code. It is reported by several references ([35], [36], [37]) that velocity-pressure coupling can cause checkerboard oscillation on the solution for central differencing. Staggered grid approach implemented for the code development. Pressure stored at the cell centers and velocity components stored in the nodes of cells which can seen by the figure 3.8. Another important characteristic in the figure 3.8 is, every index arranged in counterclockwise convention. This convention is extremely important to identify the normal direction of each control

volume edge correctly. Different stencils used for the velocity and pressure due to this staggered position grid system.

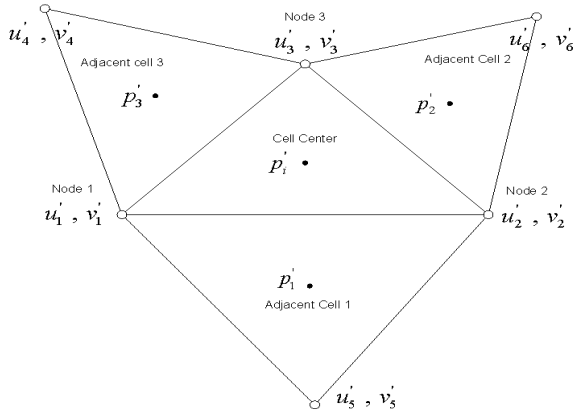

Figure 3.8. Staggered grid and counterclockwise convention

Control volume for the velocity components at nodes are chosen to be polygonal composed of arbitrary number of triangles that is presented in in figure 3.9. Convective and diffusive terms for momentum conservation, are also discretized in different stencils. Arbitrary number of cell centers around a node requires stencil to be adaptive to satisfy the any geometry in 2D. This has been successfully satisfied by an adaptive algorithm created for the interior nodes. Additionally, special algorithms developed inside the code for the implementation of boundary nodes since implementation becomes more difficult due to the combinations that may occur. An example polygonal discretization of the first order derivatives in convective terms of 3.29 and 3.30 for the tentative velocity components are given in 3.32 and 3.33 where $u^{'}$ denotes tentative velocity components. Notation for index(i) represents the node number.

$$\left(\frac{\partial u^{'}}{\partial x^{'}}\right)_c = \frac{1}{A_c}\int_{S_c} u^{'} dy^{'} = \frac{1}{A_c}\sum_{i=1}^{6} \frac{u^{'}{}_{i+1} - u^{'}{}_{i}}{2}(y^{'}{}_{i+1} + y^{'}{}_{i}) \tag{3.32}$$

$$\left(\frac{\partial u^{'}}{\partial y^{'}}\right)_c = \frac{1}{A_c}\int_{S_c} u^{'} dx^{'} = \frac{1}{A_c}\sum_{i=1}^{6} \frac{u^{'}{}_{i+1} - u^{'}{}_{i}}{2}(x^{'}{}_{i+1} + x^{'}{}_{i}) \tag{3.33}$$

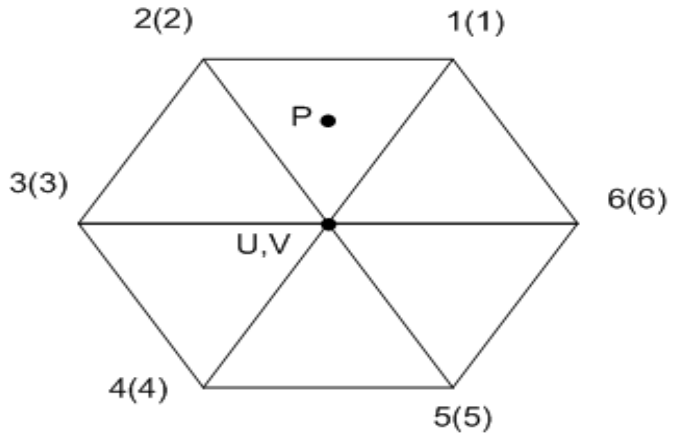

Figure 3.9. Example stencil for the convective terms

Diffusive terms are discretized according to the stencil given in figure 3.10. Discretization of these terms needs the discretization of the first order derivatives beforehand. First order derivative discretization, handled with a sub control volume, which is extracted from the control volume stencil in figure 3.10, given in figure 3.11.

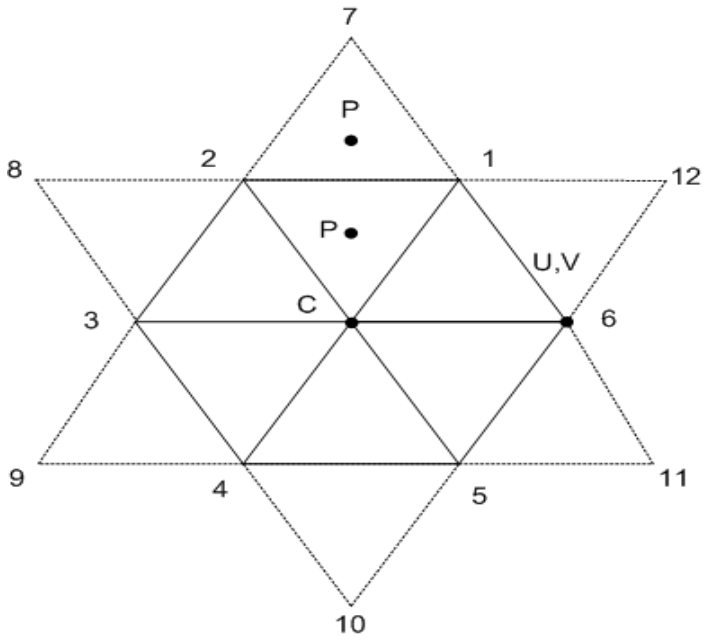

Figure 3.10. Example stencil for the diffusive terms

Discretization of the first order derivatives can be seen in equations 3.34 and 3.35 on sub control volume 3.11. Discretized first order terms are incorporated from every sub control volume segment to achieve the second order diffusive terms which can be seen in 3.36 and 3.37. Emphasized discretizations up to now can be found in reference

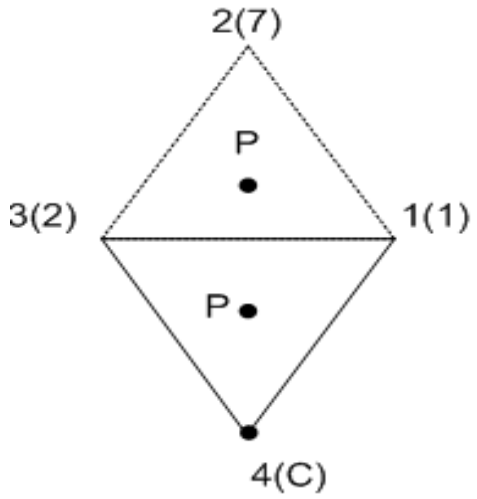

Figure 3.11. Example stencil for the sub control volume of diffusive terms

[36]. Accuracy of these discretizations are reported to be second order in the same reference. Temporal discretization implementation exactly same with equation 3.21.

$$\left(\frac{\partial u^{'}}{\partial x^{'}}\right)_{i+\frac{1}{2}} = -\frac{1}{A_{sc}}\int_{S_c} u^{'}dy^{'} = \frac{1}{A_c}\sum_{i=1}^{4}\frac{u^{'}_{i+1}-u^{'}_{i}}{2}(y^{'}_{i+1}-y^{'}_{i}) \tag{3.34}$$

$$\left(\frac{\partial u^{'}}{\partial y^{'}}\right)_{i+\frac{1}{2}} = -\frac{1}{A_{sc}}\int_{S_c} u^{'}dx^{'} = \frac{1}{A_c}\sum_{i=1}^{4}\frac{u^{'}_{i+1}-u^{'}_{i}}{2}(x^{'}_{i+1}-x^{'}_{i}) \tag{3.35}$$

$$\left(\frac{\partial^2 u^{'}}{\partial x^{2'}}\right)_{c} = \frac{1}{A_c}\int_{c}\left(\frac{\partial u^{'}}{\partial x^{'}}\right)dy^{'} = \frac{1}{A_c}\sum_{i=1}^{6}\left(\frac{\partial u^{'}}{\partial x^{'}}\right)_{i+\frac{1}{2}}(y^{'}_{i+1}-y^{'}_{i}) \tag{3.36}$$

$$\left(\frac{\partial^2 u^{'}}{\partial y^{2'}}\right)_{c} = \frac{1}{A_c}\int_{c}\left(\frac{\partial u^{'}}{\partial y^{'}}\right)dx^{'} = \frac{1}{A_c}\sum_{i=1}^{6}\left(\frac{\partial u^{'}}{\partial y^{'}}\right)_{i+\frac{1}{2}}(x^{'}_{i+1}-x^{'}_{i}) \tag{3.37}$$

Pressure terms are discretized different from the reference [36]. Poisson equation given by the equation 3.30 has been opened on a stencil given 3.12. There is a special treatment on the pressure in terms of grid points [38]. Although, pressure terms are

said to be solved on the cell centers, these pressure values are interpolated to the nodes in each iteration from the triangle centers covering around the node. These interpolated node values are used as auxiliary points for the scheme to establish the finite volume discretization on stencil giben in figure 3.30. Additionally it is remarkable to state that these interpolated points are taken on the right hand side vector(b and has not been included in the coefficient matrix A given linear system in equation 3.38. Interpolated terms will be denoted with superscript (n), defining that they have been interpolated in last known time step.

$$Ax = b \tag{3.38}$$

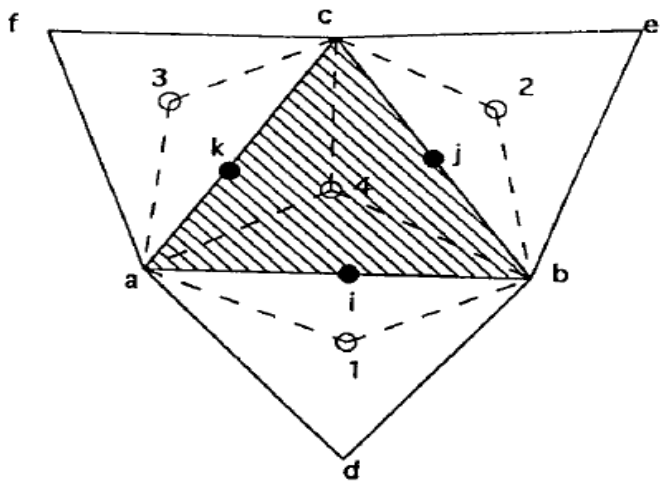

Figure 3.12. Control volume and stencil for the poisson equation

Discretization has been conducted according to the following procedure given in equations 3.39 and 3.40.

$$\left(\frac{\partial^2 p^{'}}{\partial x^{'2}}\right)_k = \frac{p_1^{'(n+1)}(y_b^{'}-y_a^{'})^2}{2A_{a1b4}} + p_a^{'n}\left(\frac{(y_1^{'}-y_4^{'})(y_b^{'}-y_a^{'})}{2A_{a1b4}} + \frac{(y_4^{'}-y_3^{'})(y_a^{'}-y_c^{'})}{2A_{a1b4}}\right)$$

$$+ \frac{p_2^{'(n+1)}(y_c^{'}-y_b^{'})^2}{2A_{b2c4}} + p_b^{'n}\left(\frac{(y_2^{'}-y_4^{'})(y_c^{'}-y_b^{'})}{2A_{b2c4}} + \frac{(y_4^{'}-y_1^{'})(y_b^{'}-y_a^{'})}{2A_{a1b4}}\right)$$

$$+ \frac{p_3^{'(n+1)}(y_a^{'}-y_c^{'})^2}{2A_{c3a4}} + p_c^{'n}\left(\frac{(y_4^{'}-y_2^{'})(y_c^{'}-y_b^{'})}{2A_{b2c4}} + \frac{(y_3^{'}-y_4^{'})(y_a^{'}-y_c^{'})}{2A_{c3a4}}\right)$$

$$+ p_3^{'(n+1)}\left(\frac{(y_b^{'}-y_a^{'})^2}{2A_{a1b4}} + \frac{(y_c^{'}-y_b^{'})^2}{2A_{b2c4}} + \frac{(y_c^{'}-y_a^{'})^2}{2A_{c3a4}}\right) \tag{3.39}$$

$$\left(\frac{\partial^2 p^{'}}{\partial y^{'2}}\right)_k = \frac{p_1^{'(n+1)}(x_b^{'}-x_a^{'})^2}{2A_{a1b4}} + p_a^{'n}\left(\frac{(x_1^{'}-x_4^{'})(x_b^{'}-x_a^{'})}{2A_{a1b4}} + \frac{(x_4^{'}-x_3^{'})(x_a^{'}-x_c^{'})}{2A_{a1b4}}\right)$$

$$+ \frac{p_2^{'(n+1)}(x_c^{'}-x_b^{'})^2}{2A_{b2c4}} + p_b^{'n}\left(\frac{(x_2^{'}-x_4^{'})(x_c^{'}-x_b^{'})}{2A_{b2c4}} + \frac{(x_4^{'}-x_1^{'})(x_b^{'}-x_a^{'})}{2A_{a1b4}}\right)$$

$$+ \frac{p_3^{'(n+1)}(x_a^{'}-x_c^{'})^2}{2A_{c3a4}} + p_c^{'n}\left(\frac{(x_4^{'}-x_2^{'})(x_c^{'}-x_b^{'})}{2A_{b2c4}} + \frac{(x_3^{'}-x_4^{'})(x_a^{'}-x_c^{'})}{2A_{c3a4}}\right)$$

$$+ p_3^{'(n+1)}\left(\frac{(x_b^{'}-x_a^{'})^2}{2A_{a1b4}} + \frac{(x_c^{'}-x_b^{'})^2}{2A_{b2c4}} + \frac{(x_c^{'}-x_a^{'})^2}{2A_{c3a4}}\right) \tag{3.40}$$

3.3. Numerical Methods

Several methods had to be incorporated with the discretization techniques that have been stated in the last chapters to get satisfactory results. Modern and robust iterative solvers have been used extensively in this study. One of the main goal was to incorporate efficient and flexible discretization with a robust iterative technique to create powerful tool. Newton-Krylov Subspace methods are implemented as the major solver. These methods has wide range of different types of solvers accompanied by the various preconditioners. SPARSKIT(A basic tool-kit for sparse matrix computations) libraries has been incorporated inside the code. Several iterative solver options to be available inside the code. Overview of the available and already tested solver and preconditioners are given in the following tables. Preconditioning can also be applied from left, right or in split form via these libraries. GMRES(Generalized minimized residual method) method with ILUT preconditioning has been found to be the most efficient combination for the governing equations that are under interest after some numerical tests. The next section states some background of this.

Table 3.1. Available Solvers

GMRES
Conjugate gradient method
Biconjugate gradient method
Biconjugate Stabilized method

Table 3.2. Available preconditioners for the subspace methods

$ILU(0)$
$MLU(0)$
$ILUT$
$ILUK$
$ILUP$
$ILUD$

3.3.1. Krylov Methods

A particularly suitable class of iterative techniques for the solution of large linear equation systems are the so-called Krylov-subspace methods. Several were proposed for the inversion of matrices which arise in CFD. Examples are the Conjugate Gradient Squared (CGS) method, Bi-Conjugate Gradient Stabilized (Bi-CGSTAB) scheme or Transpose-Free Quasi-Minimum residual (TFQMR) approach. However, the most successful Krylov subspace method became the Generalized Minimal Residual (GMRES) technique, which was originally suggested by Saad and Schulz [39]. Since then, the GMRES method was improved and augmented by several researchers.

These methods can be individually derived from optimization principles, but can also be placed together under the common framework of projection methods. Projection methods for solving $Ax = b$ determine an approximate solution x_m from m-dimensional subspace denoted by κ_m.

$$x_m = x_o + \kappa_m \tag{3.41}$$

The term x_o is an initial guess to the solution, by imposing the Petrov-Galerkin condition given by the expression 3.42 where $\mathcal{L}_m$ denote the another subspace of dimension m.

$$b - Ax_m \perp \mathcal{L}_m \tag{3.42}$$

Initial residual defined by the r_o and can be obtained by the following equation.

$$r_o = b - Ax_o \tag{3.43}$$

Krylov subspace defined by combination of coefficient matrix and initial guess as fol-

lows.

$$\mathcal{L}_m(A, r_o) = span(r_o, Ar_o, A^2 r_o, ..., A^{m-1} r_o) \tag{3.44}$$

κ_m subspace, projected over the second subspace $\mathcal{L}_m$. The main goal in this study is to minimize the two norm given by the equation 3.45 where $\mathcal{L}_m$ chosen as equation 3.46.

$$\|b - Ax_m\|_2 \tag{3.45}$$

$$\mathcal{L}_m = A\kappa_m \tag{3.46}$$

3.3.2. Preconditioning

Preconditioning transforms the system $Ax = b$ into an equivalent system, one which has the same solution but better convergence properties. Given a preconditioner M which is an approximation to A, transforms the system from left, right or split form. First two types of preconditioning given respectively by equations 3.47, 3.48.

$$M^{-1}Ax = M^{-1}b \tag{3.47}$$

$$AM^{-1}u = b, x = M^{-1}u \tag{3.48}$$

Split preconditioning needs factorization of the preconditioning matrix. The incomplete LU preconditioner obtains a factorization of M which is the close approximation of A into lower and upper triangular factors, the matrices L and U, respectively, such that the following conditions are satisfied: Matrices L and U have the same

nonzero structure as the matrix A. Nonzero elements of matrix A are equal to the corresponding element of the product LU. Implementation of this preconditioning given in the equation 3.49. This kind of preconditioning used in this study.

$$L^{-1}AU^{-1}u = L^{-1}b, x = U^{-1}u \tag{3.49}$$

3.4. Data Structure

Data structure is essebtial point for the definition of the ustructured grids. The ijk notation of the structure grids are no more valid for the unstructured grids. There should be a adressing due to this constraint. Grid generators creates these adressing system for the main to read and process. The main structure of the data structure is topological definition. Figure 3.13 shows the main topological levels of this definitions in 2D and 3D. 2D topology has been used in this study. Data structure on whole domain can be seen in the figure 3.14.

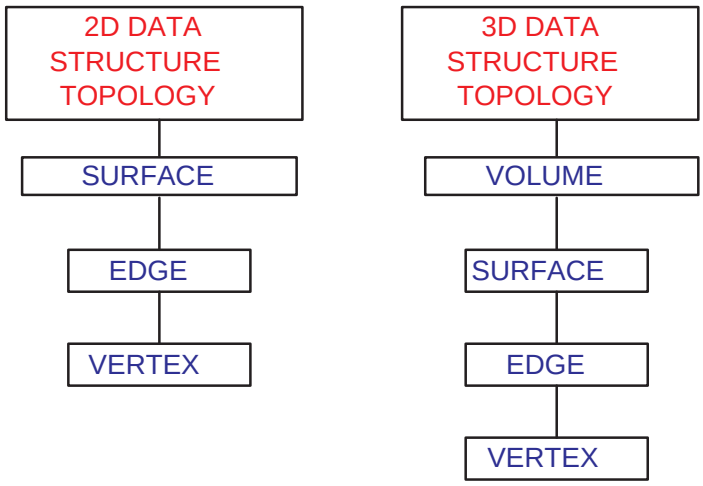

Figure 3.13. Data structure topology in 2D and 3D

Higher topological elements can be expressed by the lower ones. As an example, a line can be exrpressed by adjacent two vertex in 2D. Figure 3.15 asserts that line 67 defined by the points 100 and 58. These three number uniquely defines the address of

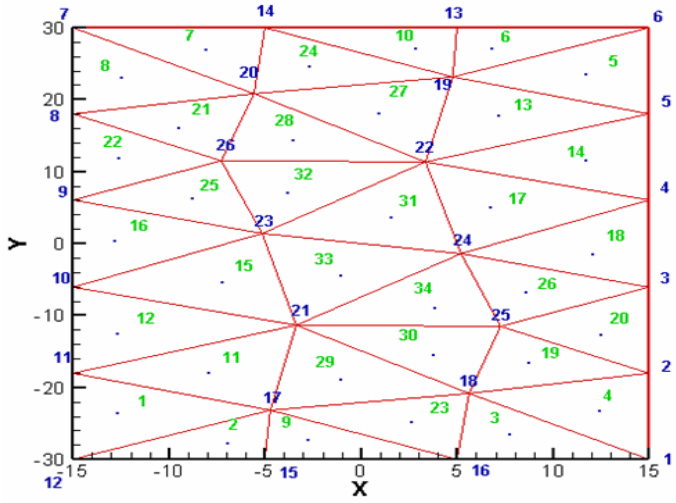

Figure 3.14. Data structure on a whole domain in 2D

the line 67 in 2D space.

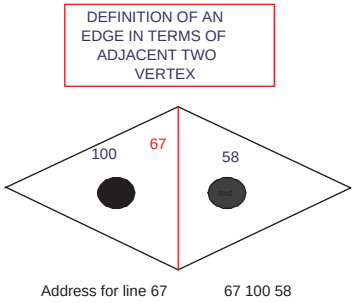

Figure 3.15. Definition of an edge by vertex

The main idea of the data structure is to construct a suitable system, which is efficient to process data during computation. The effiency determined according to the fact that one data is not processed for several times. If same operation on the data need to be made sevreal times data structure turns to be inefficent addreessing system. Another aspect of the data structure constructing is to take consideration of dicretization. Use of the adressing should take care of storing sufficient but not excessive data. If the data stored excessively, big loads can not be handle by the code whereas storing less data will lead same data to be processed several times. The optimization should be handled.

Derived data types has been used in terms of coding to handle the suitable data structure. Actually several data struture has been used due to the staggered grid ori-

entation of the physical quantities for different control volumes. Additionally different data structure used for the boundary cells. As an example, derived data type for the data structure of a triangle control volume has been used according to the figure 3.16. Two main data structures which are node and cell structures are constructed. These two are coupled to each other with id of a cell or node. The coordinates of the cells and nodes can be achieved by this. The coordinate values are used finally in discretization once value has been reached correctly.

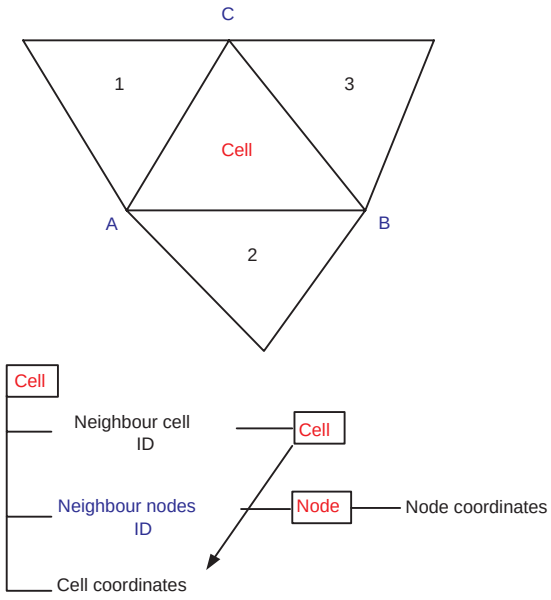

Figure 3.16. Data structure for triangle control volume

3.4.1. Storage Scheme

Storage system is one of the very important aspect that has to be considered in terms of unstructure grid system. A sparse matrix is a matrix that has very few nonzero elements. By storing and operating on only the nonzero elements, it is possible to achieve substantial savings in memory requirements and computation. In addition to the nonzero elements, storage is also required for information that determines the position of each nonzero element in the matrix. Unstructured grids has no definite sparsity pattern. An example of this random sparsity can be visualized in figure 3.17. It was essential to use such a storage system that can handle a random sparsity. The compressed row storage format(CRS) has been implemented for this purpose.

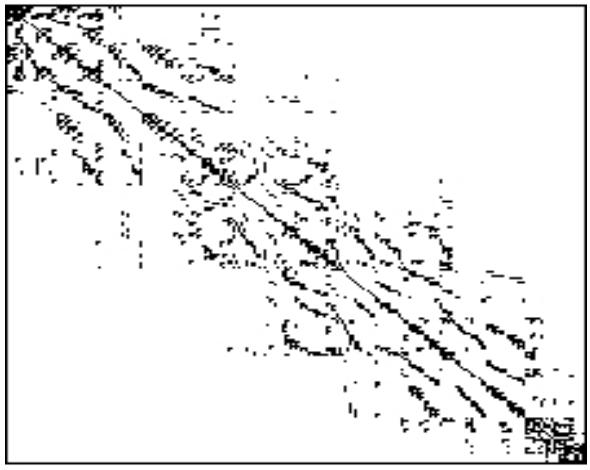

Figure 3.17. Random sparsity of unstructured grids

CRS is the most general storage system. It makes absolutely no assumptions about the sparsity structure of the matrix, and it doesn't store any unnecessary elements. CRS is basicly implemented with the following format given in figure 3.18. Each nonzero element is stored along with its row and column indices. Thus there is a single array of matrix elements, AR, along with an array of row indices, IA, and an array of the corresponding column indices, JA. As the matrix is stored by rows, the row index for all the nonzero elements in a row is stored only once. The i-th element of array IA points to the start of the i-th row in arrays JA and AR.

$$A = \begin{bmatrix} a_{11} & 0 & 0 & a_{14} & a_{15} & 0 \\ 0 & a_{22} & a_{23} & 0 & 0 & a_{26} \\ a_{31} & 0 & a_{33} & 0 & a_{35} & a_{36} \\ 0 & a_{42} & 0 & a_{44} & 0 & 0 \\ a_{51} & 0 & 0 & 0 & a_{55} & 0 \\ 0 & 0 & a_{63} & a_{64} & 0 & a_{66} \end{bmatrix}$$

$$\mathbf{AR} = (a_{11}, a_{14}, a_{15}, a_{22}, a_{23}, a_{26}, a_{31}, a_{33}, a_{35}, a_{36}, a_{42}, a_{44}, a_{51}, a_{55}, a_{63}, a_{64}, a_{66})$$

$$\mathbf{JA} = (1, 4, 5, 2, 3, 6, 1, 3, 5, 6, 2, 4, 1, 5, 3, 4, 6)$$

$$\mathbf{IA} = (1, 4, 7, 11, 13, 15, 18)$$

$$\mathbf{INDEX} = (1, 4, 7, 11, 13, 15, 18, 1, 4, 5, 2, 3, 6, 1, 3, 5, 6, 2, 4, 1, 5, 3, 4, 6)$$

Figure 3.18. Compressed row storage format(CRS)

3.4.2. Parallel Processing

Many scientific applications make use of sparse linear algebra. Because they are quite time consuming, they require an efficient parallel implementation on powerful supercomputers. The rapid advances in parallel computer architectures , with their

large aggregate memory capacity and CPU power, have reached the point were such calculations can be considered in a practical sense. This is particularly true for unstructured mesh techniques, which have been shown to scale very favorably on massively parallel machines using hundreds of processors. Massively parallel processor(MPP) architecture has been used within the context of this study. MPP composed of different processors with different memory, cache,bus and I/O devices communicated by MPI(Message Passing Interface) [41]. Interconnection of these machines established by the MPI. Example illustration of MPP given by the figure 3.19.

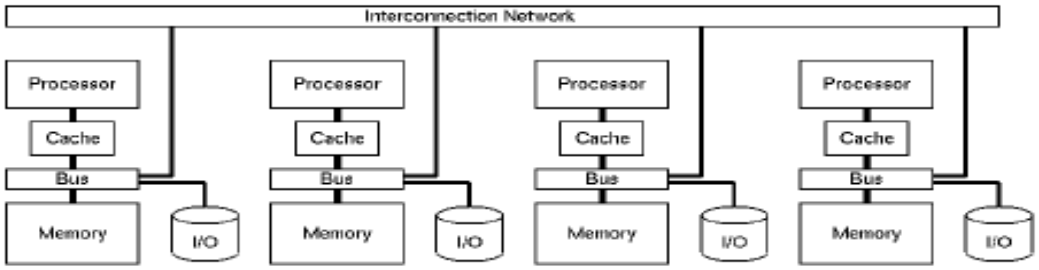

Figure 3.19. Massively parallel processor(MPP) architecture [41]

First step of parallel implementation is the domain decomposition. Domain decomposition can be made by a useful tool called METIS. METIS is a software package for partitioning large irregular graphs, partitioning large meshes, and computing fillreducing orderings of sparse matrices. METIS based on multilevel graph partitioning [40] which is a procedure of coarsening and refinement given in in figure 3.20. METIS algorithms reduce the size of the graph and then partition the smaller graph. Finally it refines the partition to obtain the partition of the given original graph.

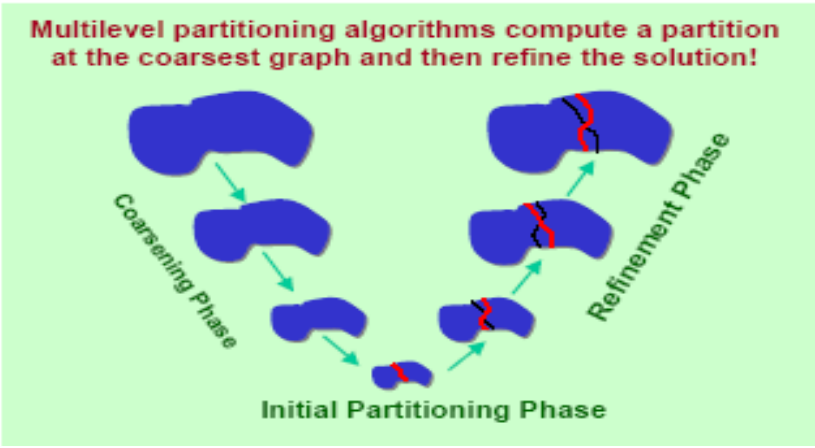

Figure 3.20. Metis methodology for grid partitioning architecture [40]

Test case problem of Taylor vortex flows between concentric cylinder implemented on the MPP cluster with at most 9 processors. Each of these processors has Pentium 4 2.0 Ghz processors with 256 mb random access memory. The partitioning of this problem made with METIS tool. The resulting partitioning of METIS for 9 processor given in the figure 3.21.

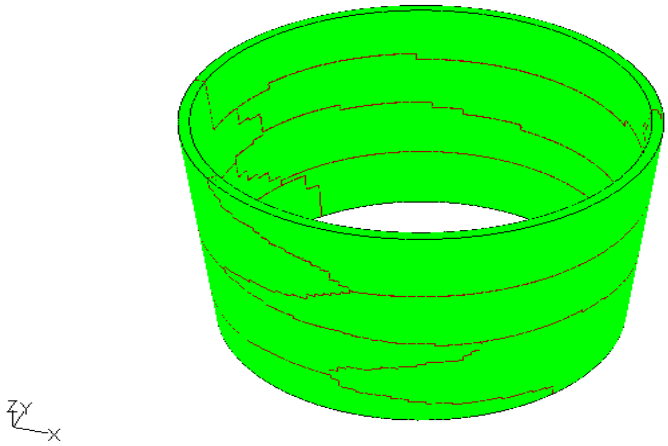

Figure 3.21. Partitioned concentric cylinders by METIS

Additionally, lid driven cavity flow has been performed in parallel in ASMA cluster with PETSc libraries. There were at most 6 processors available in the cluster for the computation. These processors were P4 2.0 Ghz with 128 random access memory.

Performance of the parallel processing determined according to some terminological terms. Speedup factor, efficiency, cost and scalability are the most important performance parameters. Definitions of these parameters are given below:

Speed up factor

$$S_n = \frac{\text{Execution time using one processor}}{\text{Execution time using a multiprocessor with n number of processors}} \tag{3.50}$$

$$= \frac{t_s}{t_p} \tag{3.51}$$

Efficiency

$$E_p = \frac{\text{Execution time using one processor}}{(\text{Execution time using a multiprocessor processors})(\text{Number of processors})} \tag{3.52}$$

$$= \frac{t_s}{t_p n} \tag{3.53}$$

Cost

$$C_p = (\text{Execution time})(\text{Total number of processors used}) \tag{3.54}$$

$$= \frac{t_s}{E_p} \tag{3.55}$$

Scalability There are different scalability definitions for the hardware or algorithmic point of view. The scalability in this study defined in terms of the algorithmic scalability. An algorithm said to be scalable if it can accommodate increased data items with low and bounded increase in computational time. This parameter can be figured out if the information about speedup factor, efficiency and cost graphs are available.

4. RESULTS AND DISCUSSION

Firstly, Grid and geometrical considerations will be stated. Boundary conditions will be emphasized following this information. Results will be validated with respect to data provided from literature. Residual history of the numerical simulation will be introduced for each case. Parallel data which has been post processed in terms of parallel processing terminological terms, inserted on charts for a further discussion.

4.1. Vortex Flows with Unstructured Grids (Code Development)

Lid driven cavity problem was defined by boundary conditions of the figure 1.14. Lid-driven cavity flow of a Newtonian fluid has occupied the attention of the scientific computational community. Over the years the problem has spawned a huge number of papers; mainly concerned with the development of computational algorithms where, in a continuous drive to demonstrate the superior accuracy and stability properties of their latest numerical method. Several researchers have applied it to one of the problems two-dimensional rectangular or three-dimensional cubic forms. This made this problem a suitable benchmark study test for a newly developed codes. Additionally, this problem chosen to be the test case due to the interaction of the vortex structures are included in the physics of the problem. Parallel implementation of this problem, which will be emphasized in a following section, also implemented. Basic flow diagram of the sequential code can be seen in figure 4.1.

4.1.1. Validation of Results

Widely used benchmark paper in literature for this test case is given by the reference [42]. The model paper of the code development [36] also uses this reference as the validation. Spectral methods has been used by this method. These methods leads convergence in the order of 10^{-20}. Convergence criteria of $5 * 10^{-7}$ has been used by this study. Residual norm history for u and v velocity at $Re = 400$ obtained by the solver given in the figures 4.2 and figures 4.3 respectively.

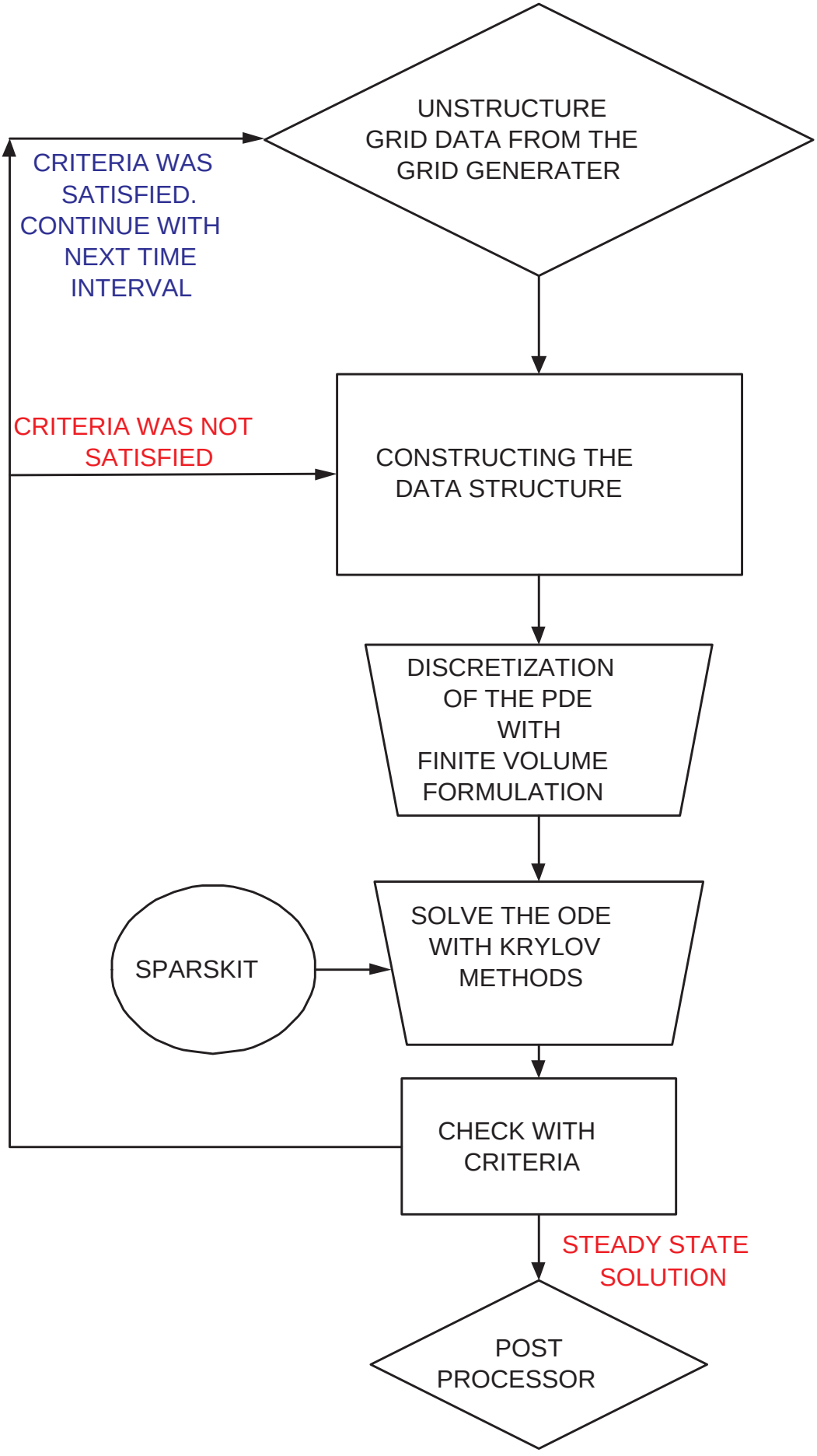

Figure 4.1. Flow diagram of the sequential unstructured grid code

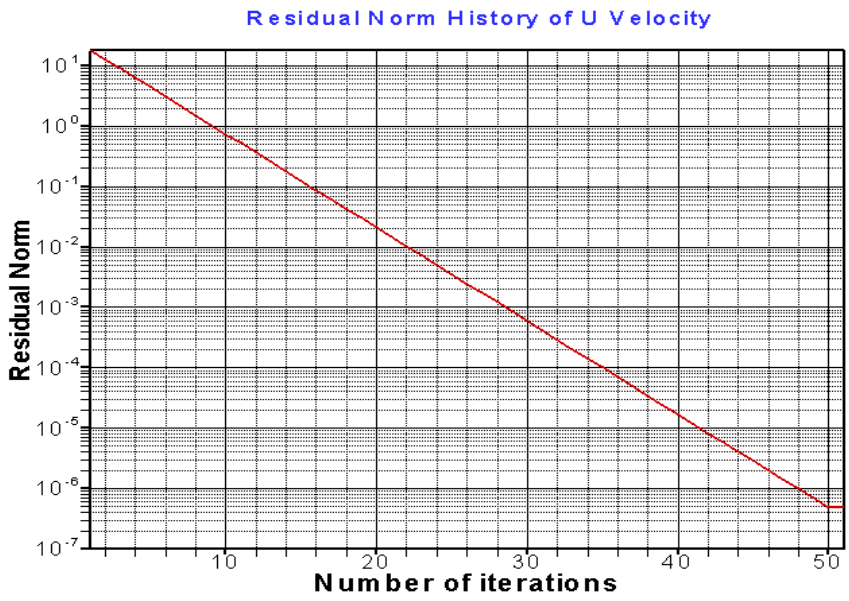

Figure 4.2. Residual norm history for u velocity at Re=400

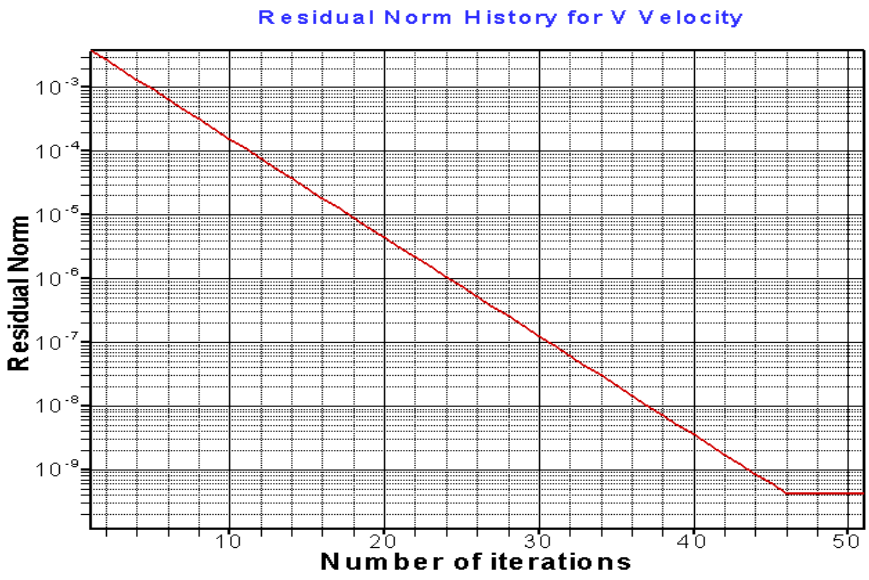

Figure 4.3. Residual norm history for v velocity at Re=400

Convergence criteria is in terms of two norm for this study. Velocity profile of horizontal direction has been extracted and compared with the reference [42] for different Reynolds numbers. Additionally pressure contours from available in reference [36] for $Re = 100$ and $Re = 400$ are compared with the results obtained by the code. Finally results are discussed in terms physical and numerical point of view. Following three subsections introduce the validations for three different Reynolds numbers.

4.1.1.1. Validation at Re=100. Stream trace and velocity vector field calculated by the solver given in the figure 4.4 for Reynolds number 100. Pressure contours are compared with the reference [36] in figure 4.6.

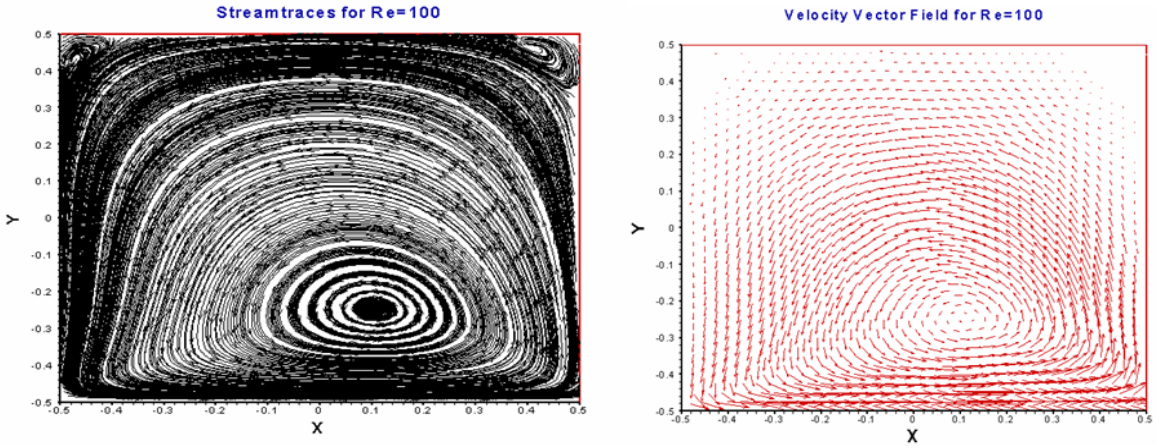

Figure 4.4. Streamtaces and velocity vectors for Re=100 at steady state

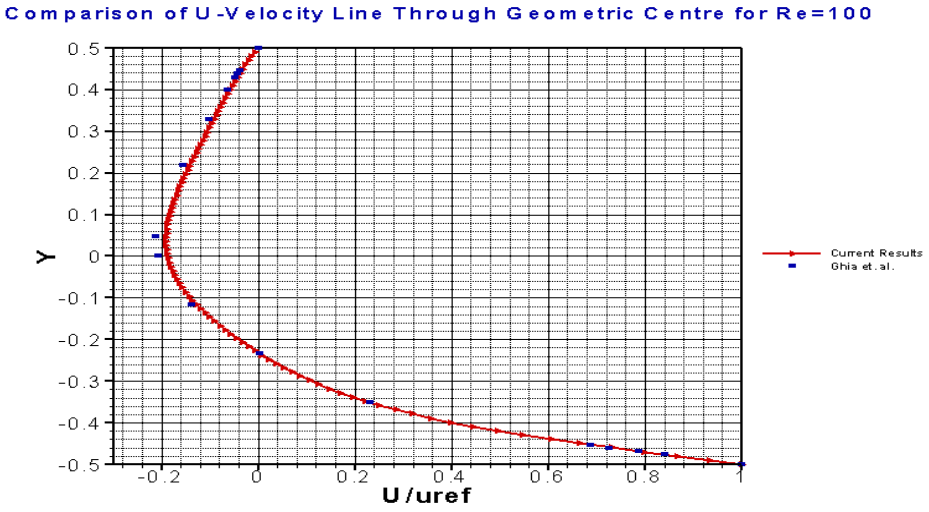

Figure 4.5. U velocity validation for Re=100 at steady state

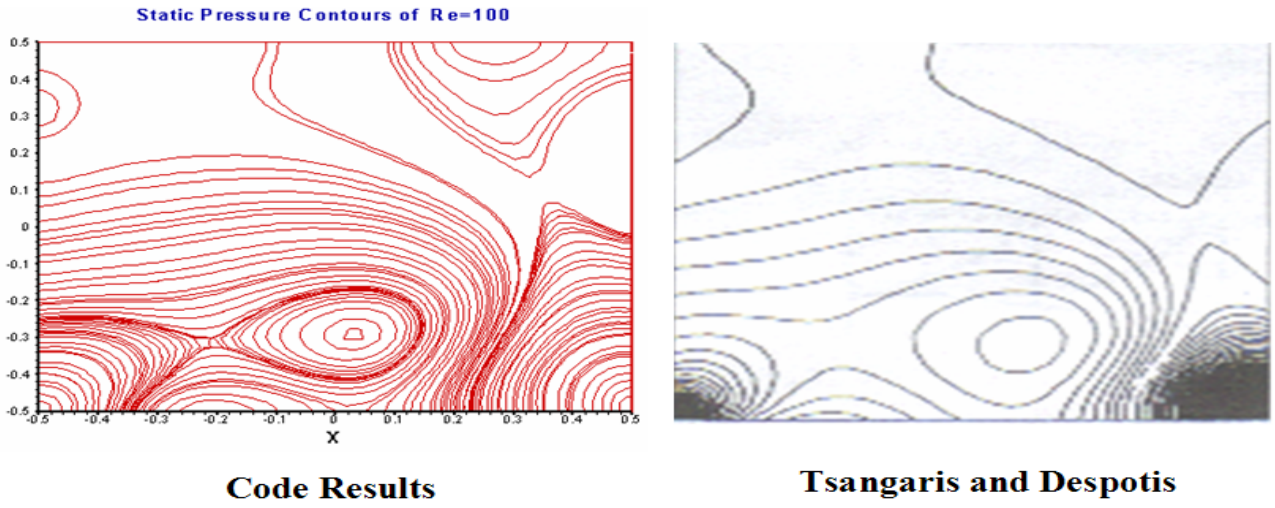

Figure 4.6. Pressure contours for Re=100 at steady state [36]

4.1.1.2. Validation at Re=400. Same validations conducted for the $Re = 400$ in same way for $Re = 100$. The validation graphics are given through figures 4.7- 4.9.

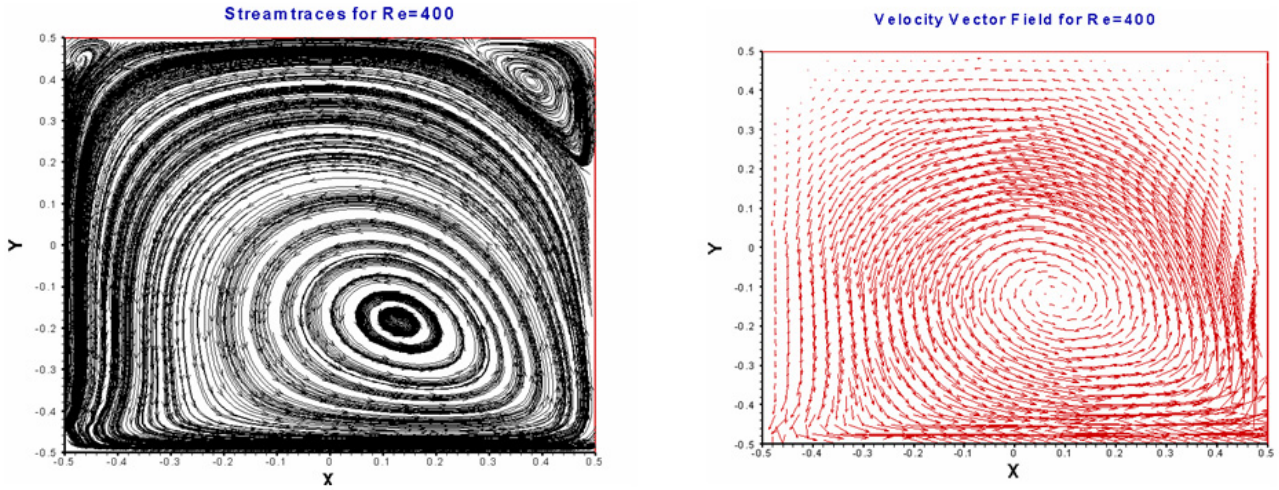

Figure 4.7. Streamtaces and velocity vectors for Re=400 at steady state

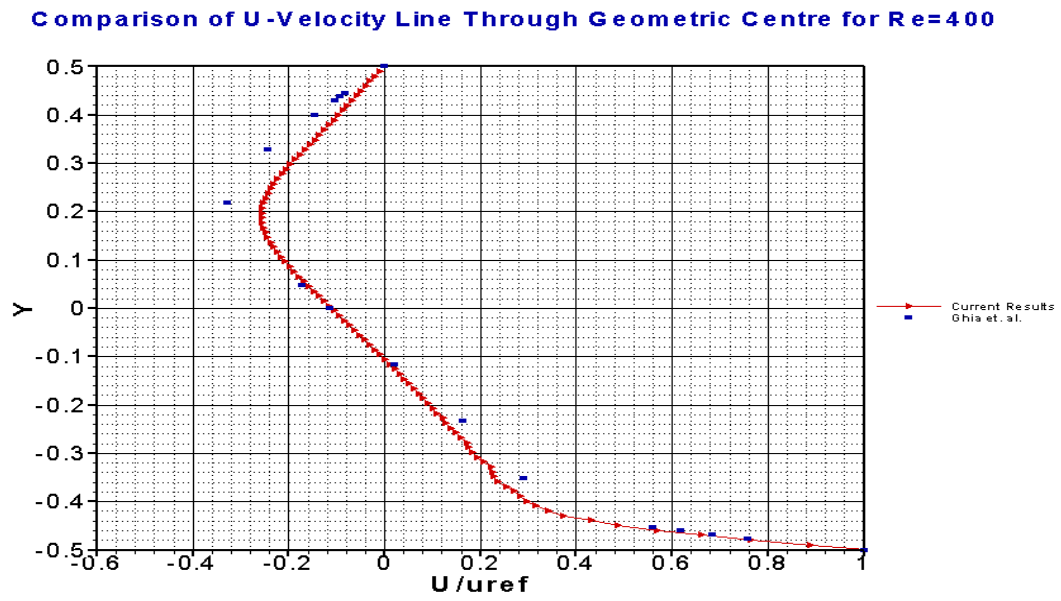

[h]

Figure 4.8. U velocity validation for Re=400 at steady state

[h]

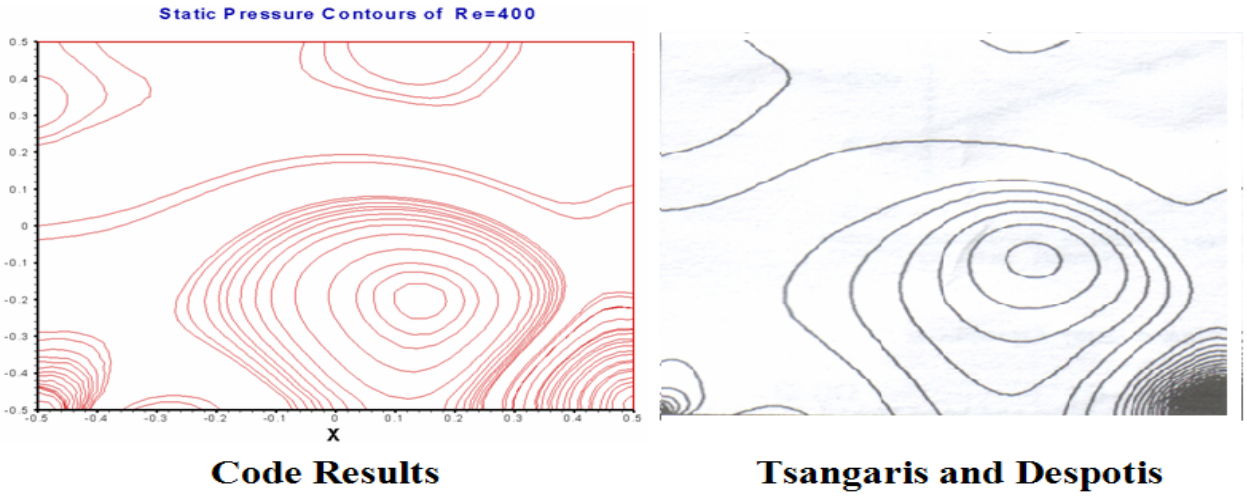

Figure 4.9. Pressure contours for Re=400 at steady state [36]

4.1.1.3. Validation at Re=1000. $Re = 1000$ is highest point which simulations conducted. There were no pressure data available for $Re = 1000$ but other validations on velocity has been conducted as seen in figure 4.11.

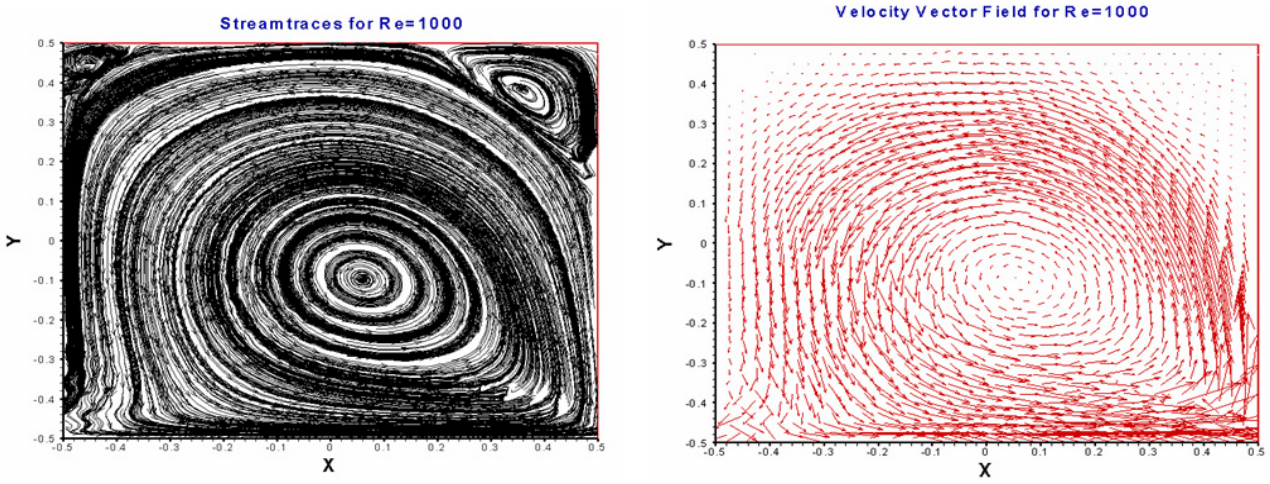

Figure 4.10. Streamtaces and velocity vectors for Re=1000 at steady state

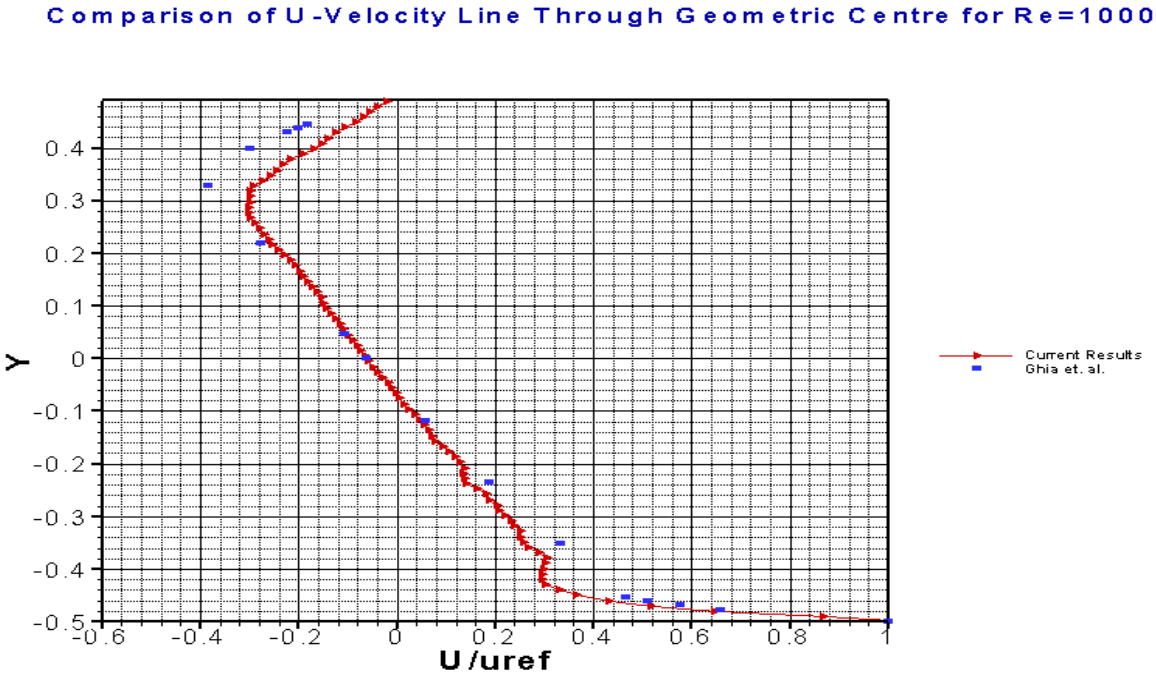

Figure 4.11. U velocity validation for Re=1000 at steady state

4.1.1.4. Discussion of Results. Reynolds number of around 100, the primary vortex moves to wards the right-hand wall and the downstream secondary eddy starts to enlarge in size. At a Reynolds number of 400, the primary vortex starts to move to

wards the cavity center and it continues to move to the center at even higher Reynolds numbers. Evidence of growth in the upstream secondary eddy at a Reynolds number of 400 is also now visible. If the Reynolds number is increased further to 1000 another secondary eddy emerges on the upper left-hand cavity wall. These three vortices are effecting to each other in a implicit form and increasing the nonlinearity. This is the point where solver and discretization starts to have problems. Solver found to be capable of providing sufficiently satisfactory results up to a high Reynolds numbers like 1000. Convergence of in terms of residual norm is smooth and very rapid. Approximately in 40 iterations solver converges to the next time step with 0.1s step size to a unchanging residual norm of $5x10^{-7}$. It is reported in [36] approximately 500 Gauss-Seidal iterations needed to converge to the next time second with 10^{-4} criteria. This study confirms that only 41 iterations sufficient to reach convergence of $5x10{-}7$. This states that the method is highly robust and efficient.

4.2. Taylor Vortex Flows

4.2.1. Taylor Vortex Array and Decay of Adjacent Vortices (Code Development)

Only one cell of the array that was previously given in figure 1.3 has been simulated. Analytic solution of decay of an eddy was given in the equation 1.1 with $k = 0$ and $q = \pi$. This leads the stream function to take the form in equation 4.1.

$$\psi = e^{-0.00887t} Cos(\pi x) \tag{4.1}$$

The flow diagram of the developed code can be seen in figure 4.12

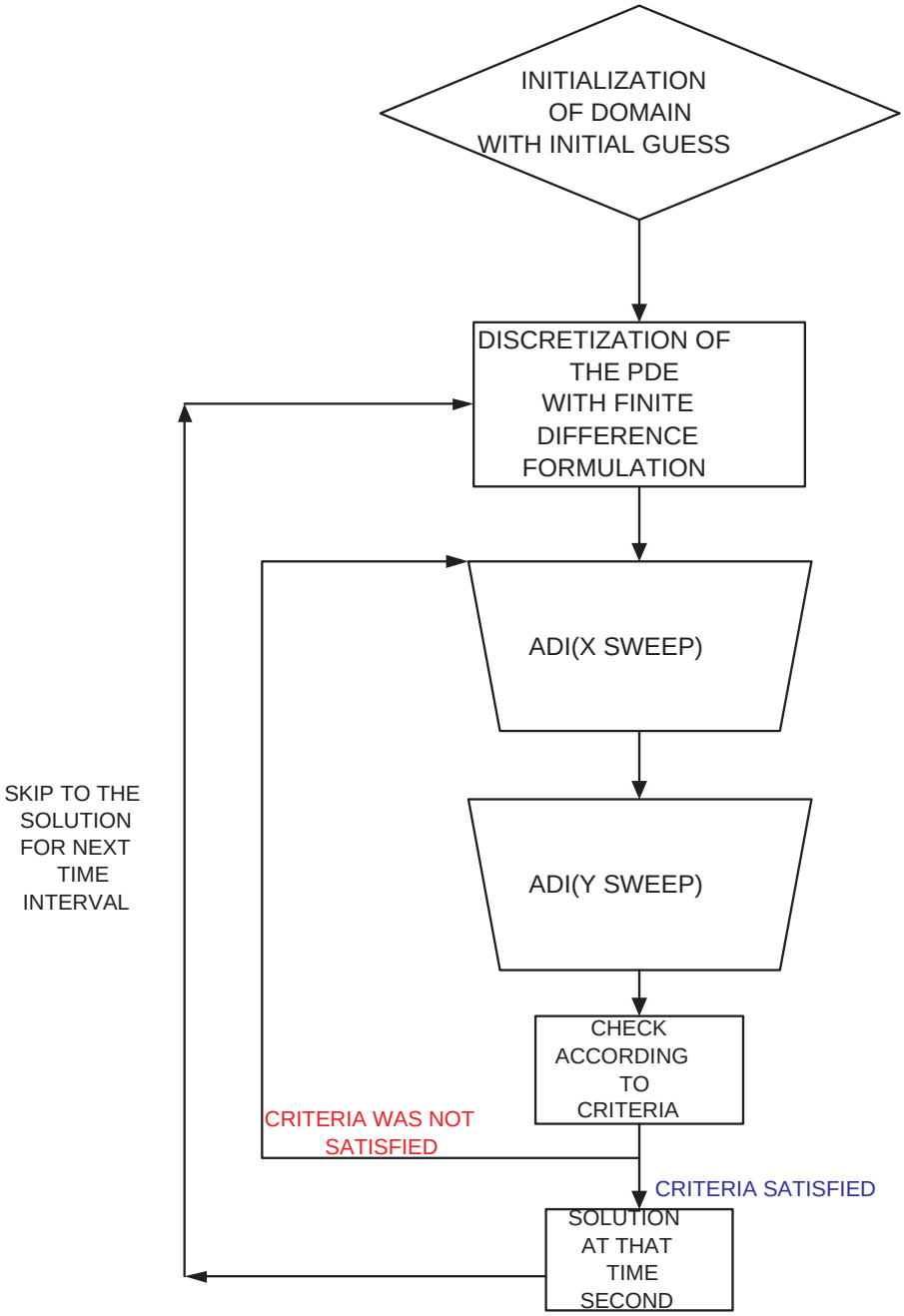

Figure 4.12. Flow chart for the code development on Taylor vortex array

Associated boundary conditions become all zero in equation 4.1 if the domain chosen as in the figure 4.13.

The error that is associated with the simulation with respect to analytical solution given by the following graph. Decay process with respect to three extracted time seconds can be visualized in figures 4.15-4.17.

, which is identically simulation of a single eddy. [h]

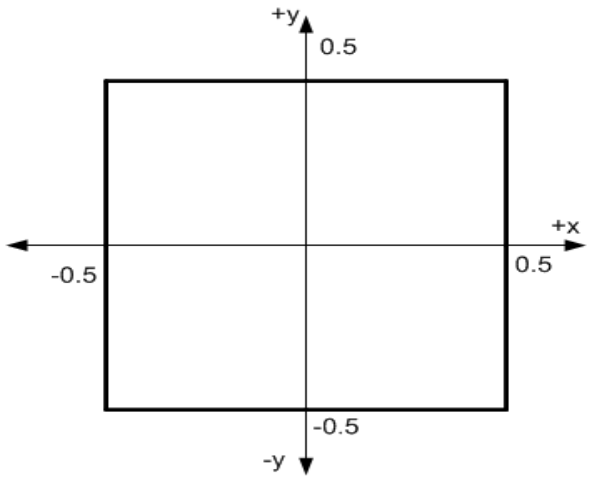

Figure 4.13. Domain for the single element of taylor vortex array

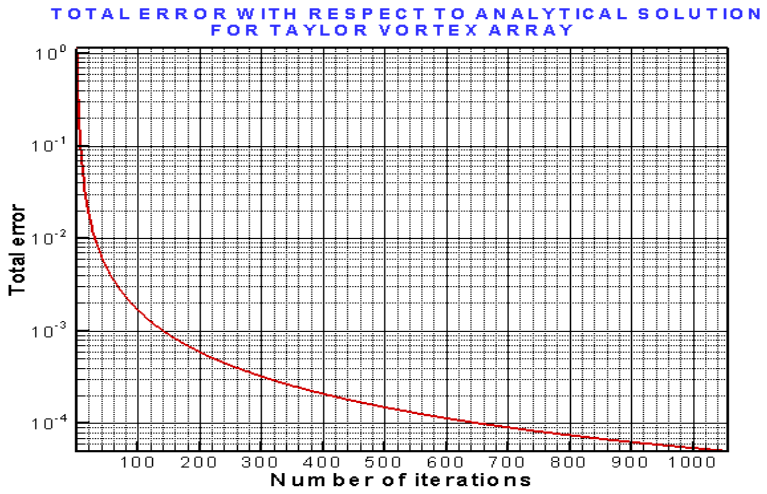

Figure 4.14. Error with respect to analytical solution

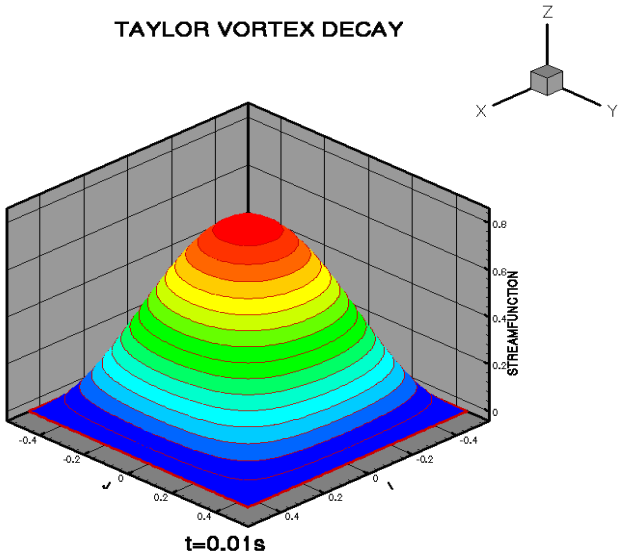

Figure 4.15. Decay of a eddy at time 0.01s

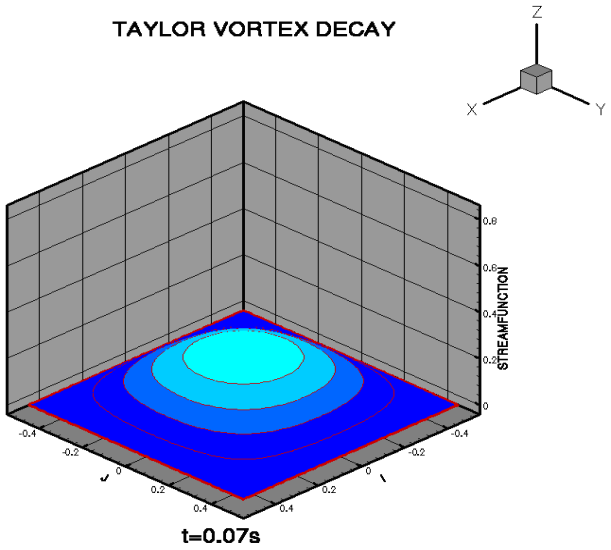

Figure 4.16. Decay of a eddy at time 0.07s

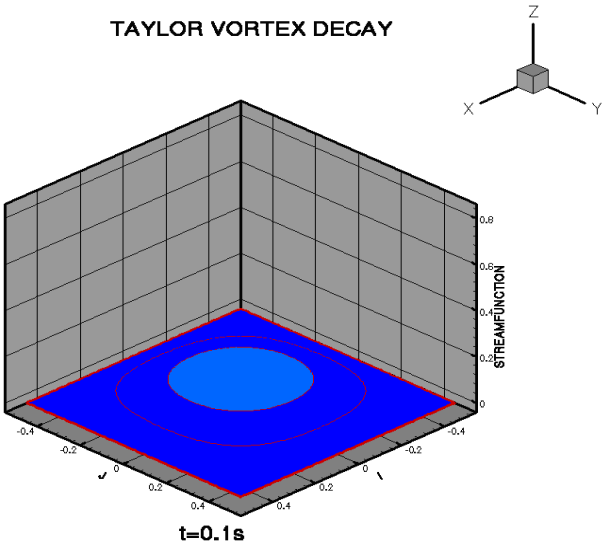

Figure 4.17. Decay of a eddy at time 0.1s

Simulation dictated that eddy totally decays in 0.12 seconds. Energy, associated by the kinetic energy inside the eddy dissipate by the viscosity. Numerical scheme converges to the total error integrated from each cell to a value of approximately order of $7x10^{-5}$. Although, numerical scheme seems to work satisfactorily, the nonlinear terms are lacking in this simulation. Introduction of highly nonlinear terms may alter the convergence dramatically.

4.2.2. Taylor Couette Flows (FLUENT Simulation)

Taylor vortex flows are interesting flows where vertical vortex formations are occurring with respect to the driven motion. The current interest of this study is to identify an analogical vortex formations on a concentric torus system. Once same vortex formations obtained, optimization for the control of these vortex structures can be established for a future implementation. This can constitute an opportunity for more efficient hydraulic systems in terms of industrial application.

Boundary conditions for the the concentric cylinder and concentric torus are same. Annular gap defined by the following expression 4.2. Annular gap(η) of 1.05 and 5 has been used for the concentric cylinders. Inner cylinder radius(r_i) is taken as 1 m. Cylinder heights are taken to be 2 m. The upper and lower walls of the concentric cylinder is stationary imposing nonslip condition.

$$\eta = \frac{r_o}{r_i} \tag{4.2}$$

The outer cylinder or torus stays silent. Inner cylinder turns with angular velocity of 25 $\frac{rad}{s}$. Taylor number (Ta) for the concentric cylinder is taken as the 3125. Re number can be identified by 1250. If the outer Reynolds number(Re_2) taken as zero and this Reynolds number taken as inner wall Reynolds number (Re_1)directly indicates that we are in Taylor vortex region in flow map was given in figure 1.6.

Firstly, validation for the Taylor vortex flow between two concentric cylinder for $\eta = 1.05$ and residual history will be indicated. Effect of the annular gap has been investigated. Secondly, it will be worthy to emphasize the relation between number of vortex formation and the annulus width between cylinders. Results of the same analysis for the concentric torus will be given in the last part.

4.2.3. Validation and Residual History

Analysis conducted for the $\eta = 1.05$. System reached steady state at time 48 s . Resolved vortex structures can be visualized from one side of cross sectional view. Vorticial structures that has been resolved from the top or bottom end walls and middle of the concentric cylinders are given in the figures 4.18 and 4.19 respectively. It is evident that the vortex that is attached to the top or bottom wall is bigger than the inner vortex structure. Reason for this can be investigated in figure 4.20, where turbulent viscosity can be visualized. It is clear that stationary wall increases the turbulent viscosity near the wall region. This extracts more kinetic energy from the flow field and consequently vortex forms in a bigger magnitude.

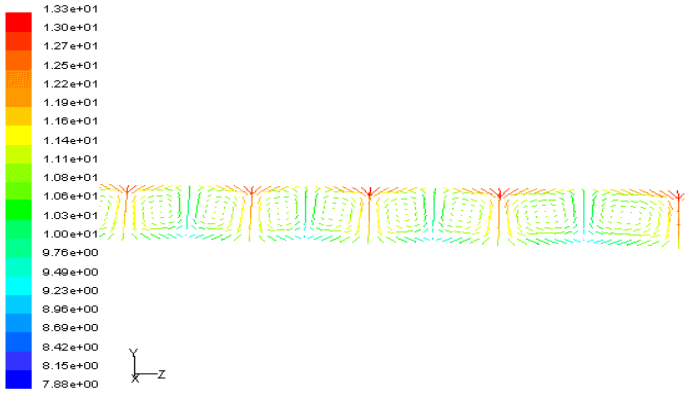

Figure 4.18. Velocity vectors at the middle of the concentric cylinders with η=1.05

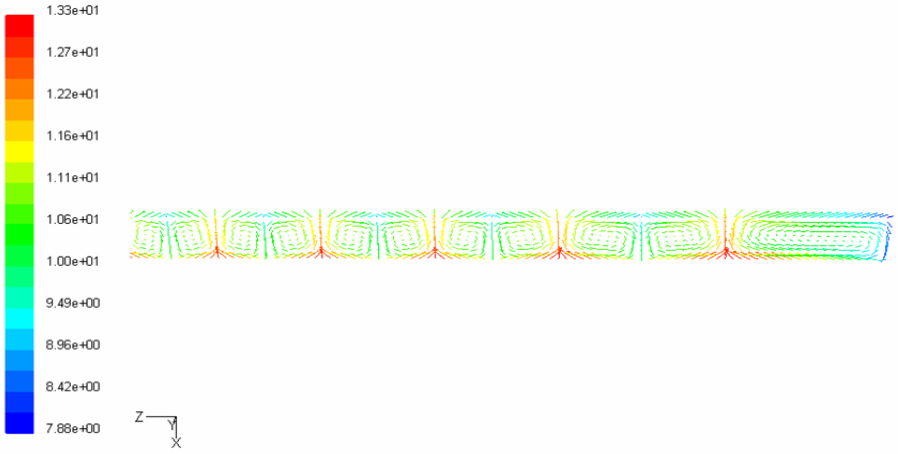

Figure 4.19. Velocity vectors at the top or bottom end walls of the concentric cylinders with η=1.05

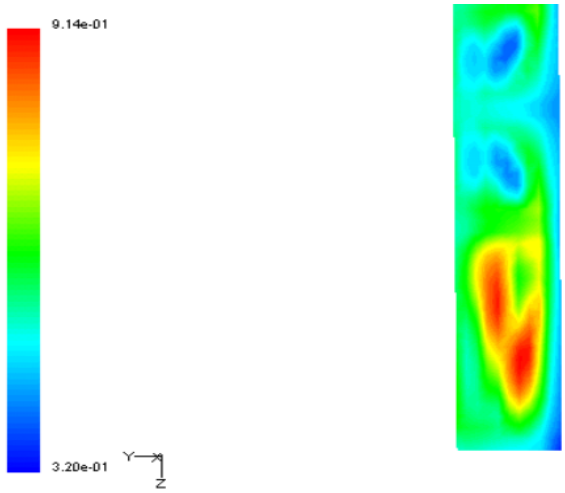

Figure 4.20. Turbulent viscosity at the top or bottom end walls of the concentric cylinders with η=1.05

Validation of these results can be established via maximum streamline amplitude history($A(t)$) in the middle plane in time from reference [43]. This concept extracted from the mid plane different time seconds till the steady state reached. This amplitude history can be seen in the figure 4.21. Similar configuration which exists in reference [43] which amplification history given with figure 4.22. It can be observed that the amplitudes and the creation history of vortex structures are similar.

$$A(t) = \psi_{max|mid} \tag{4.3}$$

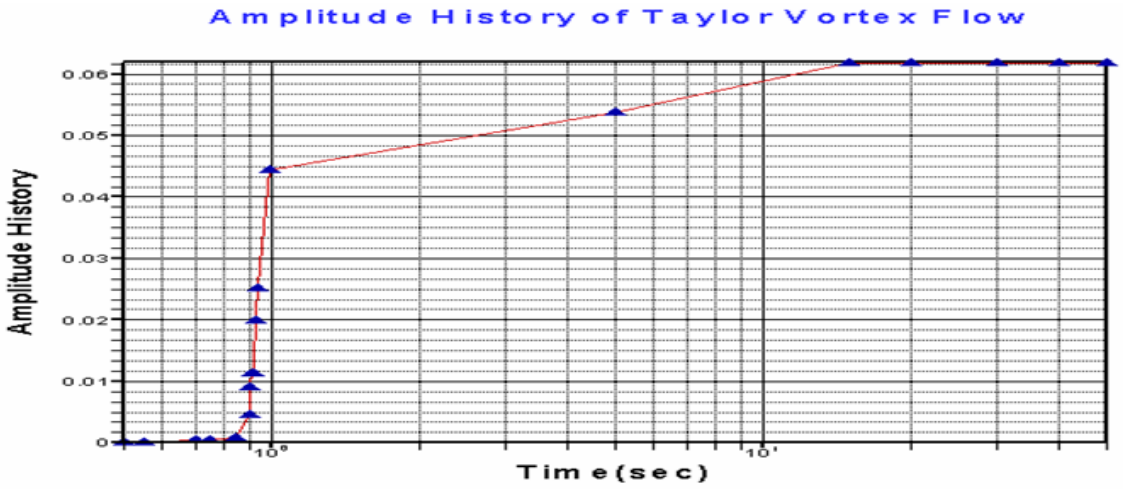

Figure 4.21. Amplitude history from the mid plane

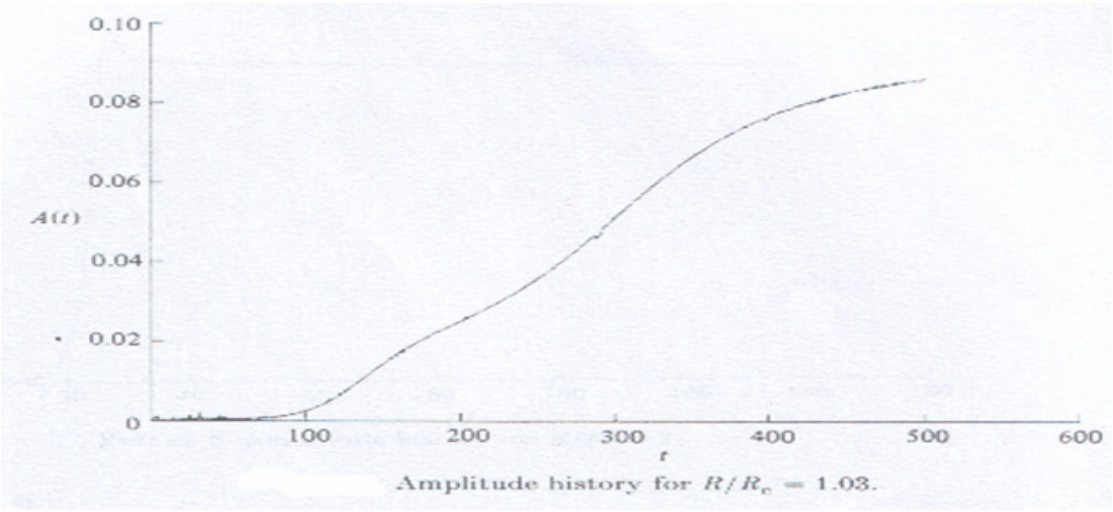

Figure 4.22. Amplitude history from the mid plane from the literature

Residual history of the system with convergence criteria of 10^{-3} can be seen in the following figure.

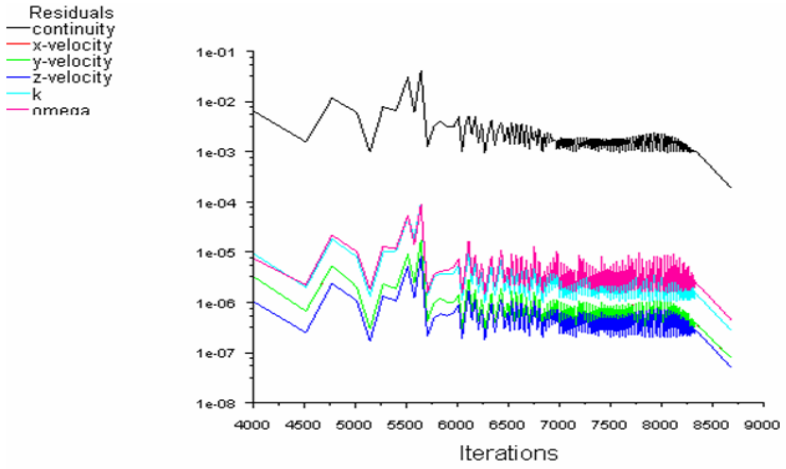

Figure 4.23. Residual history of Taylor vortex flow for concentric cylinders with η=1.05

4.2.4. Effect of the Annulus Gap

Several vortex structures has been obtained by the η of 1.05. If the same analysis with concentric cylinder keeping the cylinder height as same but changing the annular η to 5, only two big vortex formation occurs at the steady state. This can be seen

from in figure 4.24. This indicates that number of vortex structures increases by the decrease of the annulus gap.

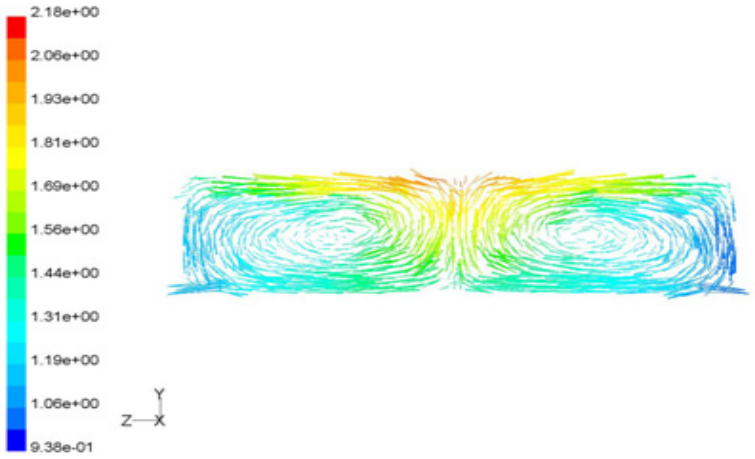

Figure 4.24. Velocity vectors of the concentric cylinders with η=5.0

4.2.5. Analysis with Analogical Concentric Torus Configuration

Concentric torus geometry with the η=2.5. Tetrahedral mesh with 248253 elements used on the geometry. System observed to reach to steady state at time step 9.9 s. Vortex structures at steady state can be visualized in figure 4.25. This analysis asserts that similar structures are forming in time in the case of torus configuration analogically to concentric cylinders.

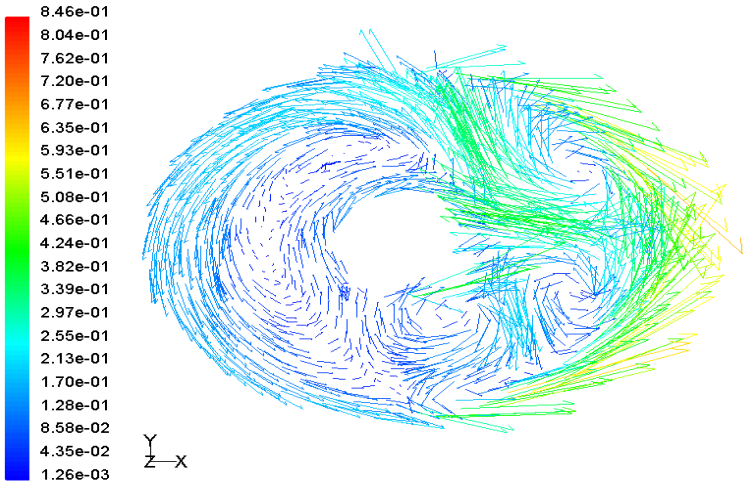

Figure 4.25. Velocity vectors of the concentric torus with η=2.5 at 9.9 s

4.3. Parallel Implementations of Vortex Flows

Parallel implementation of the vortex flows conducted for both 2D and 3D cases. Limited amount of parallel computing resources tried to be used in maximum level. Department computers are connected and configured to establish parallel processing. Taylor Vortex flows between concentric cylinders has been conducted with this cluster as test case, which uses windows operating system. Totally 9 processors found to be successively working for the simulation. Lid driven cavity problem simulated in a ASMA cluster. The interconnection network of this system was more dedicated than the department cluster. Unfortunately, the number of available processors were 6 for the parallel processing at the time simulations conducted. Results will be stated in the next subsections.

4.3.1. Parallel Simulation of Taylor Vortex Flow between Concentric Cylinders (FLUENT Simulation)

Simulation repeated for 1-9 processors. This is also repeated for three different grid levels from coarse to fine. Totally 27 simulations conducted. Each simulation starts from the initial state to the steady state. Sequential computation took 8.46, 31.47 and 34.75 hours for 120000, 270000, 325000 hexahedral grid models respectively. Maximum grid size kept as 32500 due to virtual memory requirement limit of a single processor after this limit. Terminological terms introduced in chapter 4 extracted to charts with the following figures.

Interpretation of the results reveals good results. Speedup factor of 6.2 with 9 processor obtained as maximum. This value can increase if the grid size could have been increased more or the interconnection limit can be designed in a dedicated manner. Efficiency graph in figure 4.27 states that, efficiency decreases when the number of processor increase but decrease rate slows down by the increase of the grid size. This is an indication that parallel processing can become essential technique when grid size becomes sufficiently big. Cost graphics in figure 4.28 shows always increase with the increasing processor number. Such a increase seems to be bounded to a limit value

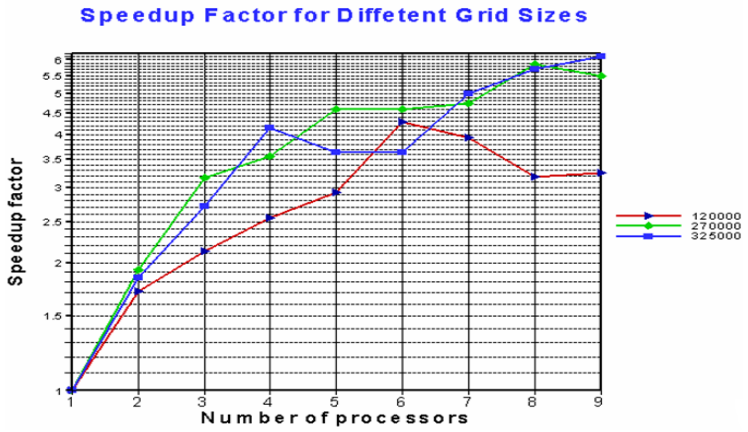

Figure 4.26. Speedup factor for concentric cylinders with η=1.05

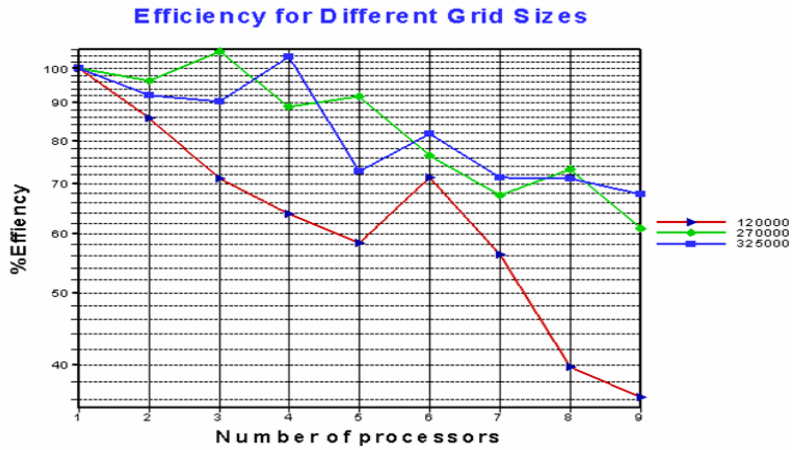

Figure 4.27. Efficiency for concentric cylinders with η=1.05

by the increase of the grid size. Increase of the grid size does not increase the cost anymore. Another important information can be provided by the data transfer rate by MPI. Following figure emphasize the data transfer per iteration for different grid sizes. Data transfer rate increase is also limited by the increasing grid size. When all these informations added up. Finally it can be stated that, simulations performed made in a scalable way.

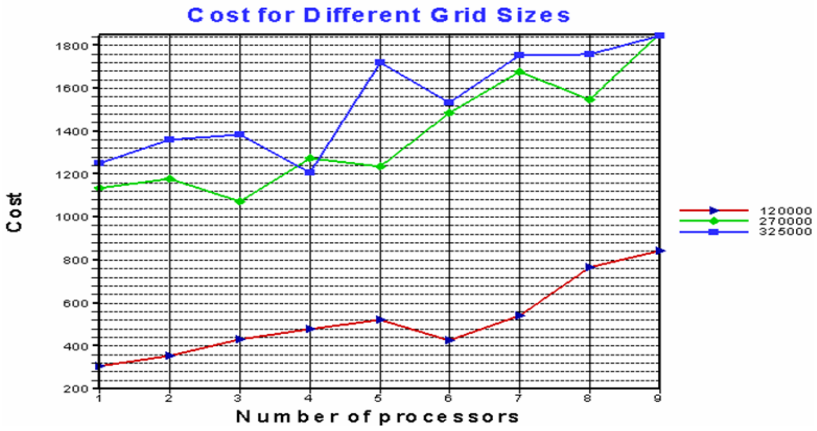

Figure 4.28. Cost for concentric cylinders with η=1.05

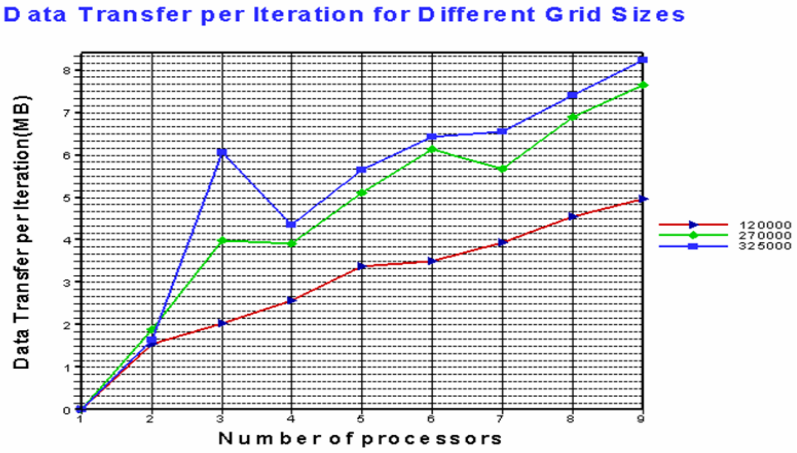

Figure 4.29. Data transfer per iteration for concentric cylinders with η=1.05

4.3.2. Parallel Simulation of 2D Lid Driven Cavity Problem (PETSc Code Development)

Lid driven cavity problem simulated in the dedicated ASMA cluster. Residual history of this simulation given in figure 4.30. Peak shows an update of the solution in the Scalable Nonlinear Equations Solvers(SNES) of PETSc tool.

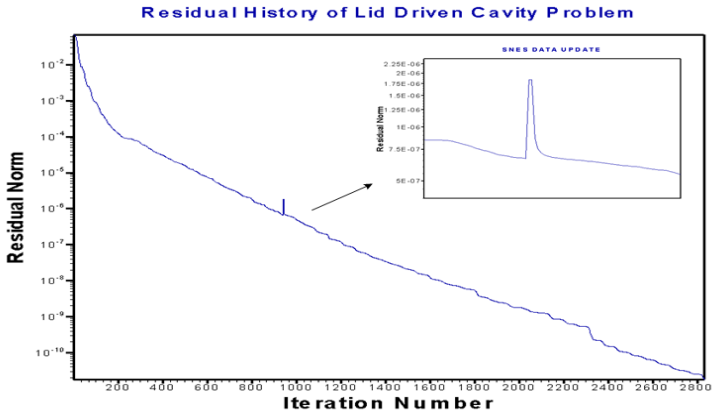

Figure 4.30. Residual history for the parallel simulation of 2D lid driven cavity problem on ASMA cluster

Results that will be given in here is important because they symbolize the effect of a dedicated network on the parallelism. Terminological terms again extracted to the graphs in the following figures.

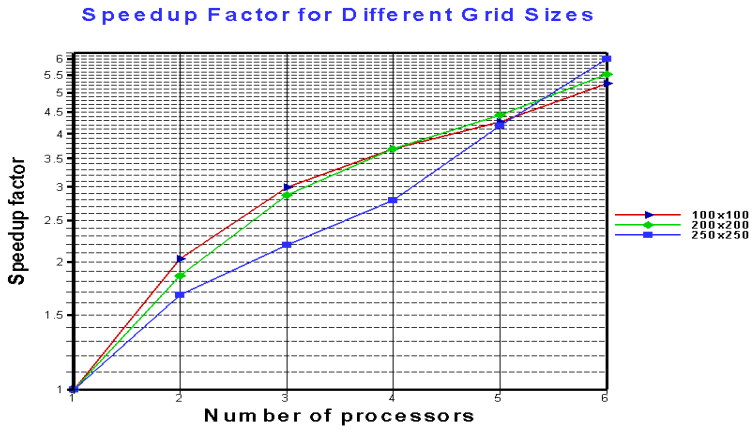

Figure 4.31. Speedup factor for 2D lid driven cavity problem

Speedup figure shows that parallelism is always beneficial in the case of a dedicated interconnection network. Efficiency decrease again takes effect with the increasing processor number. Cost is even not increasing by the increase of the number of

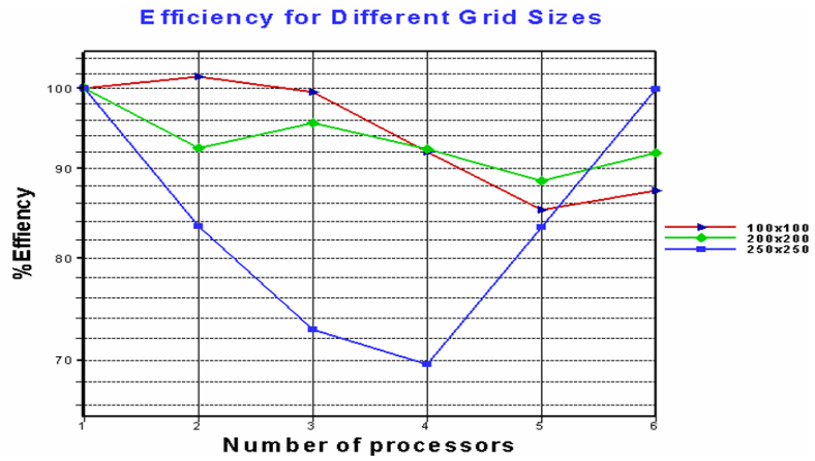

Figure 4.32. Efficiency for 2D lid driven cavity problem

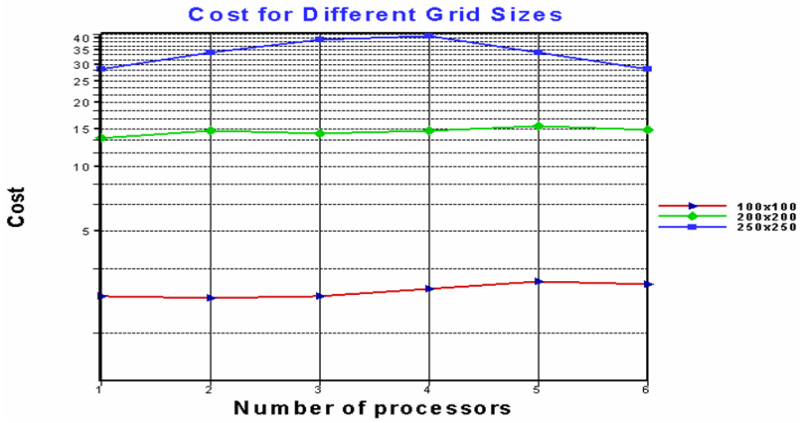

Figure 4.33. Cost for 2D lid driven cavity problem

the processors. Additionally, increase in the magnitude of cost with respect to grid size seems to become bounded as the grid size increases in figure 4.33. Results of the simulation reveals that the dedicated network can increase the performance of parallel processing technique dramatically. Unfortunately it is not possible to derive more information from these charts due to limited amount of processors that had to be used.

4.4. LES Simulation on a 3D Centrifugal Pump (FLUENT Simulation)

Centrifugal pump impeller investigated at the design load at a Re=$1.4x10^6$. Impeller were turning with 725 rpm speed. Mass inflow rate to the impeller was 3.06 $\frac{l}{s}$. The Flow is no more vortex flow in this range, but turbulent. It was very complex to handle such a problem. Reference [20] simulates only two passage accompanied with experimental data feeded in the boundaries in each time step, where this study simulates all six passages without any experimental data. Additionally, vortex identification on the final flow field has been established to extract the coherent structures.

Geometrical model of the impeller can be visualized in the figure 4.34. Grid that is generated has 1100000 hexahedral elements. Generating the grid was very difficult on the channels due to changing height of the impeller passage and essential stretching on the wall. View of the grid can be seen in figure 4.35.

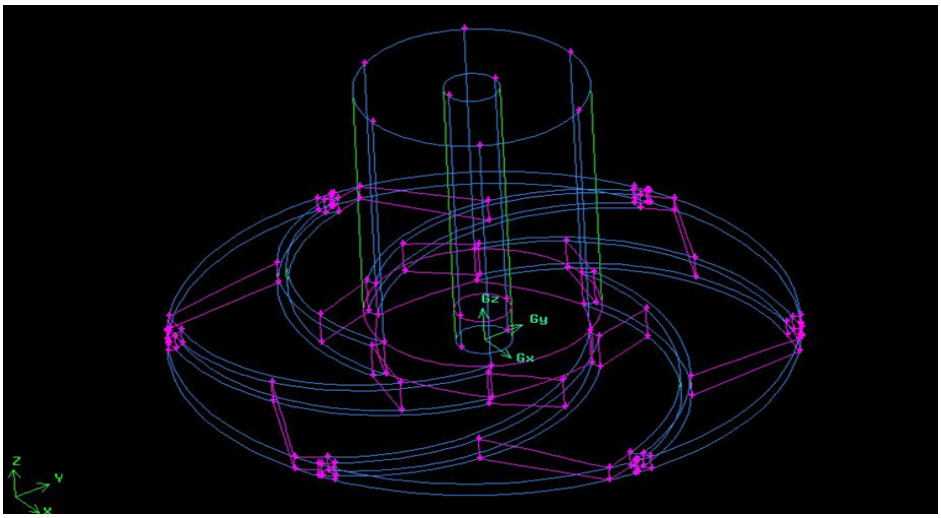

Figure 4.34. Geometrical model of centrifugal pump impeller

Time step that is used by the solver was 10^{-5} s. Simulations continued for three months to the time second of 7 s. It was possible to solve the system with convergence criteria of 10^{-5} with the generated grid. Time constraints of the study allowed only 10^{-3} criteria to be used.

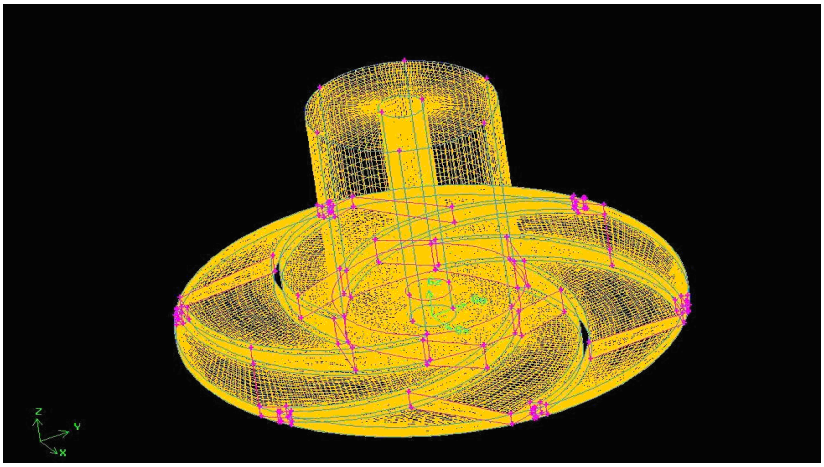

Figure 4.35. Grid generation on centrifugal pump impeller

4.4.1. Validation of the Results

Results tried to be validated at the r/R_2=0.5 station for scaled radial and tangential PIV(Particle Image Velocimetry) data available in reference [12]. Following figures are giving the validations. Since this station locates just after the leading age of the impeller blade, validations preferred at this station.

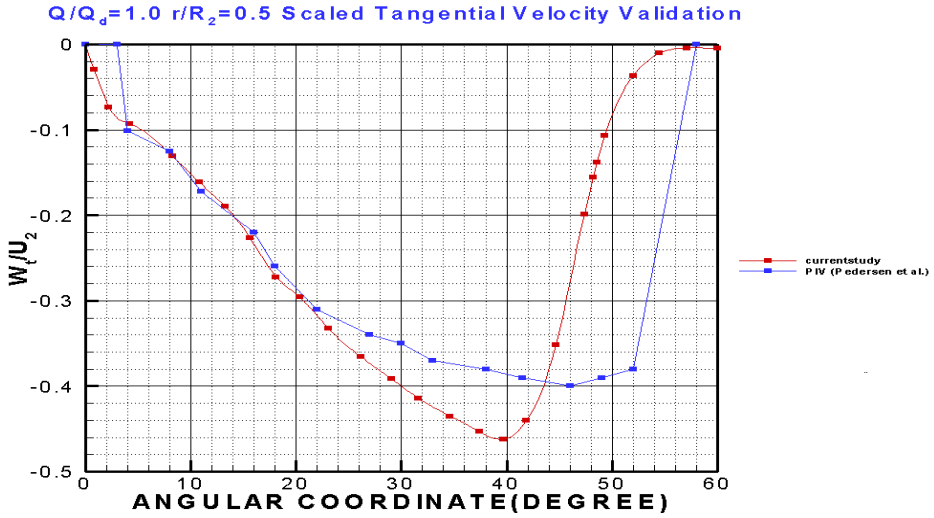

Figure 4.36. Scaled tangential velocity validation at station r/R_2=0.5 with respect to PIV data

Although, results are showing some poor results it gives at least some idea about the maximum values of the velocity to be expected. It is worthy to note that the average velocity magnitude achieved at the outflow section is calculated as 3.99 $\frac{m}{s}$.

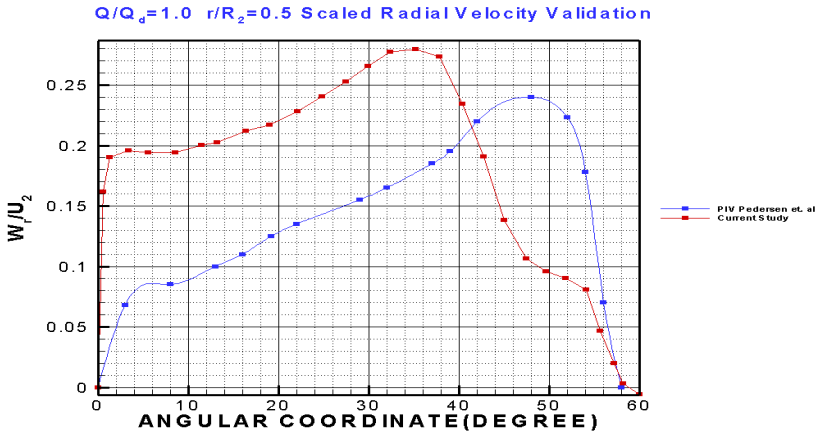

Figure 4.37. Radial velocity validation at station r/R_2=0.5 with respect to PIV data

This is very close to the value of 4 $\frac{m}{s}$ given in reference [20]. Radial velocity seems to have real problems on the basis of grid spacing in radial position. The radial data for statistical distribution is not sufficient enough to resolve the velocity field. Another problem can originate from the assumption on the convergence criteria due to time constraints. Higher tolerance on convergence directly causes insufficient numerical accuracy over 70000 time steps. This study at least encounter a first attempt for such a complex industrial flow application. Furthermore, simulation can be repeated as a future implementation to achieve better results.

4.4.2. Vortex Identification and Coherent Structures

Assuming the simulation characterize the flow field up to a some extend, vortex identification can be implemented on the flow field. Vortex identification method from the reference [44] has been coded up in a script to post process the instantaneous flow field at time second 7.018 s. All the coherent structures are given in the figure 4.38. Extracted coherent structures are refined to extract the fastest coherent structures extracted in figure 4.39.

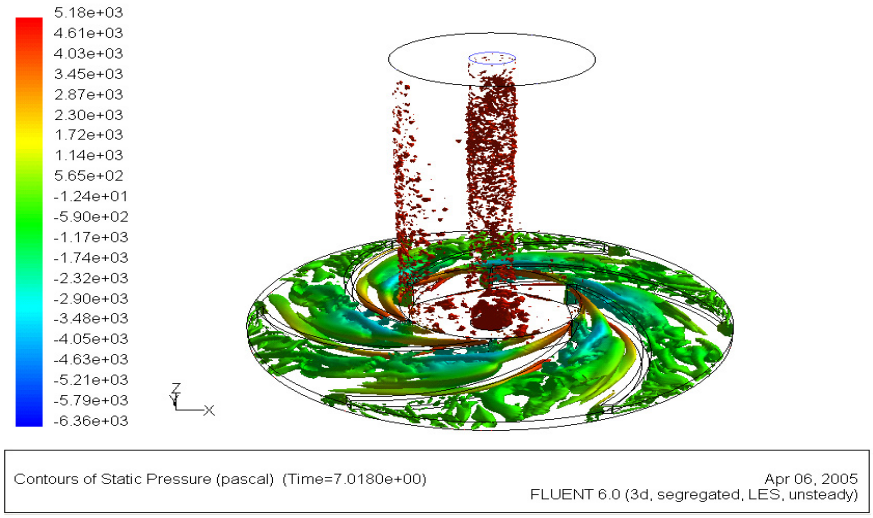

Figure 4.38. Coherent structures on centrifugal impeller at 7.018 s

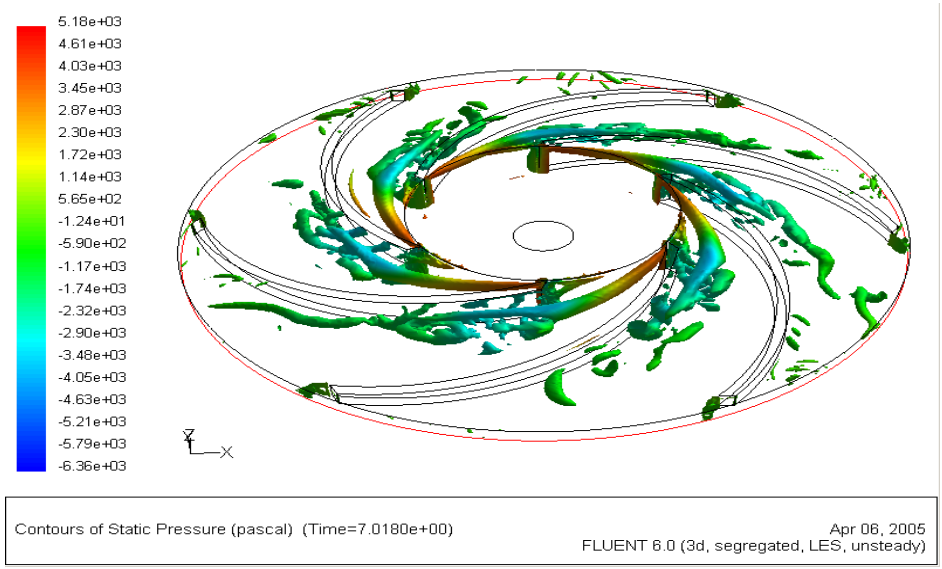

Figure 4.39. Fastest coherent structures on centrifugal impeller at 7.018 s

5. CONCLUSIONS

Several cases has been issued within the context of vortex flows in this study. Simulations has been conducted with validations to extract some valuable data for the interpretation of results and for a future implementation purpose. Unstructured code development in 2D has been established with advanced and modern numerical methods. Validation of the code development gave satisfactory results. These methods to are highly efficient and flexible and robust. Parallel processing technique introduced to the simulation to speedup the computational time. Effect of a dedicated cluster on parallel processing technique also tried to be demonstrated up to some extend. An attempt has been made to resolve turbulence on a centrifugal pump impeller which constitutes a feasibility study for a future implementation.

Finite Volume methods are used to develop an incompressible code in staggered grid arrangement, which can solve the governing equations up to high Reynolds numbers with a good accuracy. Fractional step methods used as the velocity-pressure coupling in terms of primitive variables. Code development based on the unstructured grids, which gives an opportunity to complex geometry applications. Robust solvers of Newton-Krylov methods combined with preconditioning has been implemented with success. Complex geometry applications with multi physics can be directly implemented with this code in short period of time. Domain decomposition has already been implemented on the code where parallelization can now be implemented directly. Adaptive methods and turbulence modeling may be implemented on this study on a long term period. Compressible solvers can be added to achieve all speed flow code. Algebraic multigrid methods can be another option for a further enhancement.

Decay history of a eddy simulated with a finite difference code. Limitations of the stream function-vorticity and moderate solvers which are used in this formulation stated.

Taylor vortex flows are simulated for concentric cylinder and torus geometries. Results are validated and interpreted. Analogical vortex structures in two configurations reported. These vortex formations in concentric torus medium can be studied more deeply to make an optimization on the hydraulic transmission systems. Parallel implementation of these flows performed. Results are interpreted in terms of parallel processing terminology.

An attempt has been made to resolve turbulence on a centrifugal pump impeller which constitutes a feasibility study for a future implementation. Possible enhancements on a future implementation emphasized. Vortex identification implemented on the flow field.

REFERENCES

1. Tennekes, H., J. L. Lumley *A First Course In Turbulence*, The MIT Press, England, 1972.

2. Durst, F., O. Simeon, and M. Dubravka., "Development of Fluid Mechanics Methods in the 20 th Century and the application to laminar and turbulent flow investigations", *Proceeding of the 12th International Conference on Fluid Flow Technologies*, Budapest,3-6 Sep, 1991.

3. Malalasekera, W., H. K. Versteeg *An Introduction to Fluid Dynamics The Finite Volume Method*, Longman, England, 1998.

4. Bateman, H., "The Decay of a Simple Eddy", *NACA Report 144*, 7 pp., 1923.

5. Taylor, G. I., "Stability of a Viscous Liquid Contained Between Two Rotating Cylinders", *Philios. Trans. R. Soc.*, Vol. 223, pp. 289-343, 1923.

6. Mohamed, A. G., *UCLA Academic Technology Services*, http://ats.ucla.edu/protal/joanimages/Gaber-Mohamed/page.html, Aug 2004.

7. Liao, C. S., S. J. jane, and D. L. Young, "Numerical Simulation of Three Dimensional Couette Taylor Flows", *International Journal for Numerical Methods in Fluids*, Vol. 29, pp. 827-847, 1991.

8. Sinevic, V., S. R. Kubo, and A. W. Nienow, "Power Numbers, Taylor Numbers and Taylor Vortices in Viscous Newtonian and Non-Newtonian Fluids", *Chemical Engineering Science*, Vol. 41, pp. 2915-1923, 1986.

9. Lueptow, R. M., A. Docter and K. Min, "Stability and experimental velocity field in TaylorCouette flow with axial and radial flow", *Phys. Fluids*, A. 29, pp. 2446, 1992

10. Andereck C. D., S. S. Liu, and H. L. Swinney, "Flow regimes in a circular Couette system with independently rotating cylinders", *cylinders, Journal of Fluid Mechanics*, Vol. 164, pp. 155-183, 1986.

11. HOWDENBUFALLO, *Getting to know Gyrol Fluid Drives*, http://www.howdenbuffalo.com/Products/geting20to

12. Pedersen, N. P. S. Larsen, and C. B. Jacobsen, "Flow in a Centrifugal Pump Impeller at Design and Off-Design ConditionsPart I: Particle Image Velocity (PIV) and Laser Doppler Velocimetry (LDV) Measurements", *Journal of Fluids Engineering*, Vol. 125, pp.73-83, January 2003.

13. Akin, O., and D. Rockwell, "Flow Structure in a Radial Flow Pumping System Using High-Image-Density Particle Image Velocimetry", *ASME J. Fluids Eng.*, Vol. 116, pp.538-544, 1994.

14. Eisele, K., Z. Zhang, and M. V. Casey, "Flow Analysis in a Pump DiffuserPart 1: LDA and PTV Measurements of the Unsteady Flow", *ASME J. Turbomach.*, Vol. 119, pp.968-977, 1997.

15. Sinha, M., and J. Katz, "Quantitative Visualization of the Flow in a Centrifugal Pump With Diffuser VanesI: On Flow Structures and Turbulence", *ASME J. Fluids Eng.*, Vol. 122, pp.97-107, 2000.

16. Sinha, M., J. Katz, and C. Meneveau, "Quantitative Visualization of the Flow in a Centrifugal Pump With Diffuser VanesII: Addressing Passage- Averaged and Large-Eddy Simulation Modeling Issues in Turbomachinery Flows", *ASME J. Fluids Eng.*, Vol. 122, pp.108-116, 2000.

17. Oldenburg, M., and E. Pap, "Velocity Measurements in the Impeller and in the Volute of a Centrifugal Pump by Particle Image Displacement Velocimetry", *Symposium on Applications of Laser Techniques to Fluid Mechanics*, Lisbon, Portugal, pp. 8.2.18.2.5, 1996.

18. Hayami, H., S. Aramaki and T. Watanabe, "PC-PIV System for a Measurement of Relative Flow in a Rotating Impeller Impeller",*The Second International Workshop on PIV97-Fukui*, Fukui, Japan, pp. 105108, 1997.

19. Aramaki, S., and Hayami, H., "Unsteady Flow Measurement in a Rotating Impeller Using PIV",*Proceedings of the 3rd International Workshop on PIV*, Santa Barbara, CA, pp. 1618, Sep 1999.

20. Byskov, R. K., C. B. Jacobsen, and N. Pedersen, "Flow in a Centrifugal Pump Impeller at Design and Off-Design ConditionsPart II: Large Eddy Simulations", *ASME J. Fluids Eng.*, Vol. 125, pp.73-83, January 2003.

21. Eggels, J. G. M., "Direct and Large Eddy Simulation of Turbulent Fluid Flow Using the Lattice-Boltzmann Scheme", *Int. J. Heat Fluid Flow*, Vol. 17, pp.307-323, 1996.

22. Revstedt, J., L. Fuch, and H. Trägård, "Large Eddy Simulations of the Turbulent Flow in a Stirred Reactor", *Chem. Eng. Sci.*, Vol. 53(24), pp.4041-4053, 1996.

23. Song, Ch., and X. Chen, "Simulation of Flow Through Francis Turbine by LES Method",*XVIII IAHR Symposium on Hydraulic Machinary and Cavitation*, Dordrecht, Netherlands, 1, pp. 267276, 1996.

24. Chen, X., Ch. C. S. Song, K. Tani, K. Shinmei, K. Niikura, and J. Sato, "Comprehensive Modeling of Francis Turbine System by Large Eddy Simulation Approach ", em Hydraulic Machinary and Cavitation, H. Brekke, C. G. Duan, R. K. Fisher, R. Schilling, S. K. Tan, and S. H. Winnoto, eds., World Scientific, Singapore, 1, pp. 236244, 1998.

25. Kato, C., H. Shimizu, and T. Okamura, "Large Eddy Simulation of Unsteady Flow in a Mixed-Flow Pump",*3rd ASME/JSME Joint Fluids Engeneering Conference*, New York, USA, pp. 18, 1999.

26. Sahin, M., Owens R. G., "A novel fully implicit Finite volume method applied to the lid-driven cavity problemPart I: High Reynolds number flow calculations", *Int. J. Numer. Meth. Fluids*, Vol. 42, pp.57-77, 2003.

27. Anderson, J. D., *Computational Fluid Dynamics*, McGraw-HILL, Inc., Singapore, 1995.

28. Benocci, C., *An Introduction to Mechanics of Turbulence*, VKI, 2004.

29. *Fluent 6.1 Users Manual*, Fluent Inc., Belgium, 2003.

30. Simonis, E., "An efficient multi-domain approach to large-eddy simulation of incompressible turbulent flows in complex geometries", *PhD Dissertation*, VKI, 2002.

31. Hoffmann, G., "Engineering Application of Large Eddy Simulation Turbulent Free and Wall-Bounded Shear Layers", *PhD Dissertation*, VKI, 1996.

32. Me′tais, O., *Large-Eddy Simulations of turbulence*, Laboratoire des Ecoulements Geophysiques et Industriels (LEGI), 2000.

33. Hoffmann, K. A., T. C. Steve, *Computational Fluid Engineering for Engineers Volume I*, Second Edition, Engineering Publication System, 1993.

34. McDonald, P.W., "The Cornputatdon of Transonic Flow through Two- Dimensional Gas Turbine Cascades", *ASME Paper*,71-GT-89, 1971.

35. Blazek, J., *Computational Fluid Dynamics:Princibles and Applications*, First Edition, Elsevier, 2001.

36. Despotis, G. K., S. Tsangaris, "Fractional Step Method for Solution of incompressible Navier-Stokes Equations on Unstructured Triangular Meshes", *Int. J. Numer. Meth. Fluids*, Vol. 20, pp.1273-1288, 1995.

37. Fue-Sang. L., "A pressure-based unstructured grid method for all-speed flows",

Int. J. Numer. Meth. Fluids, Vol. 33, pp.355-374, 2000.

38. Hoffmann, K. A., and T. C. Steve, *Computational Fluid Engineering for Engineers Volume II*, Second Edition, Engineering Publication System, 1993.

39. Saad, Y., and M. H. Schulz, "GMRES: A Genemlized Minimum Residual Algorithm for Solving Nonsymmetric Linear Systems", *SIAM J. Sci. Stat. C O I*, Vol. 7, pp. 856-869, 1986.

40. Karypis, G., and V. Kumar, *METIS A Software Package for Partitioning Unstructured Graphs, Partitioning Meshes, and Computing Fill-Reducing Orderings of Sparse Matrices Version 4.0*, September 1998.

41. Aoyama, Y., and J. Nakano, *RS/6000 SP: Practical MPI Programming, IBM*, August 1999.

42. Ghia U., Kh. Ghia, and CT. Shin, "High-Re solutions for incompressible flow using the NavierStokes equations and a multigrid method", *Journal of Computational Physics*, Vol. 48, pp.387-411, 1982.

43. Neitzel G. P., "Numerical Computation of Taylor Vortex flows in finite length geometries", *Journal of Fluid Mechanics*, Vol. 141, pp.51-66, 1984.

44. Jeong, J., and F. Hussain, "On the identification of a vortex", *Journal of Fluid Mechanics*, Vol. 285, pp.69-94, 1995.